https://doi.org/10.15407/ufm.26.04.756

S.V. KVON*, V.Yu. KULIKOV,**
S.K. ARINOVA*, and A.A. TUGANBAYEVA******
Abylkas Saginov Karaganda Technical University,
56 Nursultan Nazarbayev Ave., 100003 Karaganda, Kazakhstan

* s.kvon@ktu.edu.kz, ** v.kulikov@ktu.edu.kz,
*** s.arinova@ktu.edu.kz, **** dicosia0789@gmail.com

CURRENT STATE OF RESEARCH IN THE FIELD OF HIGH-ENTROPY ALLOYS' PRODUCTION IN GLOBAL PRACTICE

Metallic multicomponent high-entropy alloys (HEAs) represent a novel class of materials, which are currently the focus of extensive research. This article reviews the evolution of studies in the field of HEAs and identifies potential application areas for these materials. Recent investigations are discussed, particularly addressing the influence of various elements on the properties of HEAs with different base compositions, the formation of their microstructures, and developments in alloy design. The analysis indicates that HEAs are predominantly manufactured from pure metal powders using advanced and complex technologies such as plasma sintering and magnetron sputtering. To reduce the production costs of HEAs compared to conventional materials, increasing attention is being directed towards the development of so-called quasi-high-entropy alloys (QHEAs). The fundamental approach to creating QHEAs is analogous to that used for HEAs: a multicomponent system comprising at least five elements. However, strict equiatomic concentrations are not maintained, and requirements for charge materials and melting processes are considerably relaxed. This strategy enhances the commercial viability of QHEAs, while retaining properties comparable to those of HEAs.

Keywords: high-entropy alloy (HEA), quasi-high-entropy alloy (QHEA), equiatomic concentration, ferroalloys, production cost.

Citation: S.V. Kvon, V.Yu. Kulikov, S.K. Arinova, and A.A. Tuganbayeva, Current State of Research in the Field of High-Entropy Alloys' Production in Global Practice, *Progress in Physics of Metals*, **26**, No. 4: 756–795 (2025)

1. Introduction

High-entropy alloys (HEAs) are currently defined as alloys containing at least five components in either equiatomic concentrations or concentrations ranging between 5% and 35%, according to various sources. The principle underlying the development of HEAs diverges significantly from traditional alloy design. Conventionally, new materials are developed by alloying a principal element forming a matrix with other elements. Strengthening mechanisms in such alloys are typically based on the formation of new phases within the matrix.

In contrast, HEAs lack a principal matrix element; each component contributes equally to the formation of the alloys' structure and properties.

HEAs are produced exclusively from pure metals using technologically advanced processes, including mechanical alloying, plasma sintering, and multiple remeltings under protective atmospheres. These complex methods lead to the high production costs of HEAs, which limit their widespread use and diminish their commercial appeal.

2. Analysis of Global Trends in the HEAs Research

HEAs represent a significant trend in the advancement of structural metallic materials.

Traditionally, new alloys are developed by designing compositions based on a primary element, achieving the desired properties through alloying and subsequent processing. This methodology produces a structure comprising a matrix embedded with phases of varying origins, compositions, and structures.

By contrast, HEA development employs a fundamentally different approach. Alloy compositions typically contain at least five components, preferably in equiatomic proportions or with each element comprising between 5% and 35%. This results in a unique principle of structure formation, wherein no single component forms a dominant matrix. The contribution of each element to the overall structure is equivalent and determined by the alloys' composition.

The conceptual basis for HEA development is the thermodynamic principle of entropy maximisation through the mixing of diverse components. This process is accompanied by a reduction in free energy, which promotes the formation of simple, stable structures such as substitutional solid solutions. In most HEAs, a single-phase substitutional solid solution forms with a simple f.c.c. or b.c.c. lattice [1].

A considerable body of research has been devoted to the development of HEAs based on various systems. Interest in HEAs stems from their exceptional properties, including enhanced strength, corrosion resistance, wear resistance, and cryogenic performance, which significantly surpass those of conventional materials.

The superior properties of HEAs are attributed to the substantial lattice distortions that occur when substitutional solid solutions incorporate elements with significantly different atomic radii, leading to the enhancement of multiple material characteristics [2].

Studies [1–4] provide comprehensive reviews of HEA development, properties, and structural characteristics.

Reference [1] offers an extensive overview of HEAs, covering the historical background, thermodynamics, structural classifications, and mechanical properties of these alloys. According to Refs. [2, 3], the unique properties of HEAs are primarily associated with four key effects: the high entropy effect, the lattice distortion effect, the sluggish diffusion effect, and the 'cocktail effect'.

The high entropy effect hypothesises that the enhanced properties of HEAs arise from increased entropy in multicomponent systems with equiatomic compositions or systems containing at least five elements. The entropy of mixing in such systems is considerably higher than that observed in traditional solid solutions or intermetallic phase formations.

The lattice distortion effect is based on the involvement of atoms of varying natures that do not conform to conventional rules of solid solution formation, such as the Hume-Rothery rules.

Figure 1 presents a schematic illustration of atom arrangements and resultant lattice distortions in both conventional alloys and HEAs.

As shown in Fig. 1, atoms of other elements in conventional alloys are surrounded by atoms of the solvent element. In contrast, HEAs lack a dominant component, with atoms of all constituents occupying equivalent positions, thereby increasing entropy.

Diffusion in HEAs is generally considered to proceed at a sluggish rate [5]. This hypothesis is supported by observations of stable nanocrystalline and amorphous phases forming during HEA solidification.

The term 'cocktail effect' was first introduced in Ref. [6] to describe the properties of various materials, including amorphous metallic glasses and HEAs. This effect reflects the synergistic enhancement of properties resulting from the combination of multiple components, yielding superior properties in the final product compared to those of the individual elements. The cocktail effect accounts for the concurrent improvements in strength and ductility observed in HEAs.

Figure 2 depicts variations in thermodynamic parameters, such as Gibbs free energy and enthalpy, during the formation of regular and subregular solid solutions.

As indicated in Fig. 2, the minimum free energy in regular solutions corresponds to equiatomic compositions. In subregular solutions, the lowest free energy and, thus, the most stable phase occur at compositions deviating from equiatomic proportions. This phenomenon explains why equiatomic concentrations are rarely observed in subregular solutions.

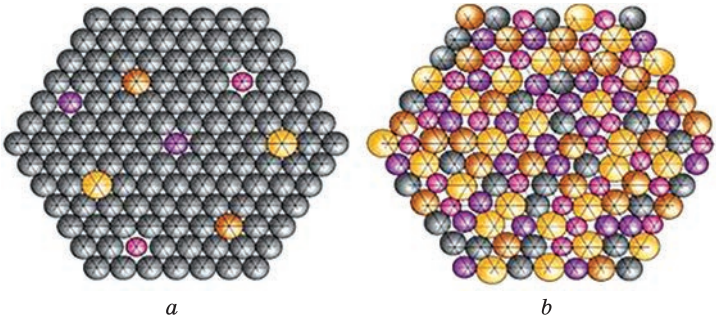

Fig. 1. Illustration of atom arrangements in a conventional alloy (*a*) and in an HEA (*b*) [1]

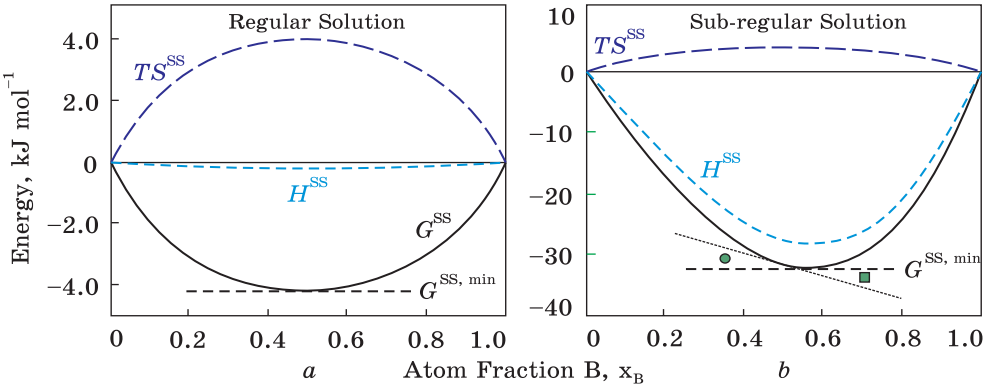

Fig. 2. Illustration of changes in thermodynamic characteristics during the formation of regular (*a*) and subregular (*b*) solutions [1, 7]

During thermodynamic analyses of HEAs, it is often argued [8–10] that the formation of HEAs violates the Gibbs phase rule. However, the author of Ref. [1] unequivocally demonstrates that the Gibbs rule determines only the maximum number of phases that can coexist at equilibrium under specified conditions. In binary systems, equilibrium microstructures are typically observed at room temperature. Single-phase solid solution regions are considerably larger than, for instance, intermetallic inclusions, leading to the conclusion that HEAs generally exhibit one or two phases.

In more complex systems such as HEAs, achieving the maximum number of equilibrium phases predicted by the Gibbs rule is practically improbable. Therefore, the actual number of phases observed in HEAs is usually lower than the theoretical maximum. This does not violate the Gibbs rule but rather confirms the potential for the formation of phases other than solid solutions.

Early HEA research posited that their exceptional properties stemmed solely from solid solutions exhibiting significant lattice distortion yet maintaining thermodynamic stability. However, recent studies [11–14] have revealed the presence of additional phases, including intermetallic and electronic compounds. Furthermore, the greater the number of elements

present in an HEA, the higher the number of observed phases, aligning with the predictions of the Gibbs rule.

Studies [1, 3, 4] report on the parameters of over 408 HEAs and provide a classification based on their compositions. The most common HEAs typically contain five or six elements, with certain elements frequently appearing across multiple alloys in this classification.

According to this classification, HEAs can be categorised into seven groups.

The first group comprises alloys based on *d*-transition metals. At least four elements from the set Al, Co, Cr, Cu, Fe, Mn, Ni, Ti, and V are included in the HEAs of this group [12, 15, 16–19]. The classic example is the Cantor alloy [12] based on the CoNiCrFeMn system.

It should be noted that, among the elements commonly found in HEAs, iron is the most prevalent, followed by manganese. More recent studies [20, 21] have investigated variants of the Cantor alloy incorporating additional elements such as V, Mo, B, and Cu.

Alloys within this system represent the next stage in the evolution of high-alloy steels, including austenitic, martensitic, and DH-strengthened steels. These alloys have attracted considerable research interest due to their potential commercial viability and specific application prospects under certain conditions.

The second group of HEAs is based on refractory metals, including Cr, Hf, Mo, Ti, V, Ta, W, and Zr [22–27]. Alloys in this category are reported less frequently in the literature and, according to Ref. [1], constitute approximately 7% of the total number of studied HEAs.

This lower prevalence is attributed to factors such as the increased complexity of fabrication due to the high melting points of the components and the reduced availability of the initial elements.

The group of HEAs based on light elements such as Al, Be, Mg, Ti, Zn, and others is associated with the development of new materials possessing low density. Research into the properties and development of alloys in this group includes studies such as [28], which addresses HEAs based on the AlFeMgTiZn system. As demonstrated by the authors of this study, HEAs within this system, produced from powder materials through mechanical alloying, exhibit high hardness and strength combined with low density.

The authors of Ref. [29] investigated the structure of HEAs based on the AlMgLiZnCu/Sn system and showed that the structure is multiphase, containing not only a large proportion of disordered solid solution but also a significant quantity of intermetallic compounds, thereby aligning these alloys more closely with the structures of conventional alloys.

Alloys of the next group are based on the AlCuMnNiSnZn system and correspond to alloyed bronzes and brasses. The design principle involves the creation of solid solutions with consideration for equiatomic concentration; therefore, their composition can be expressed by the general for-

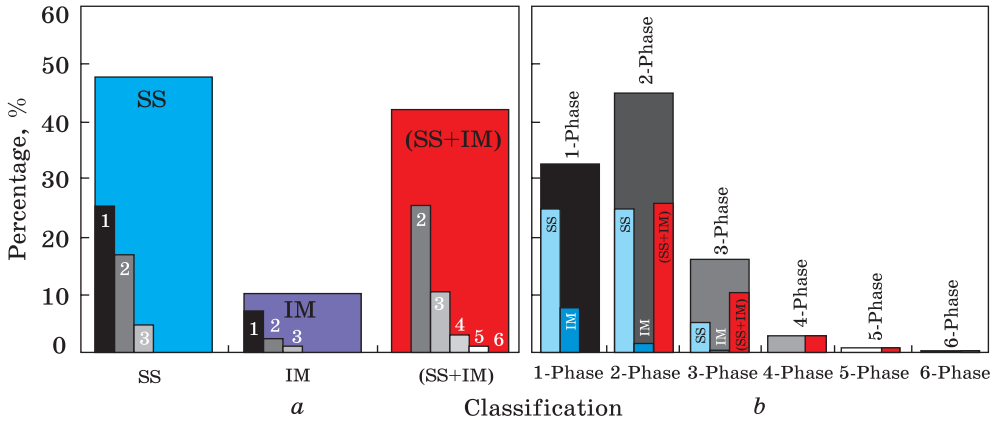

Fig. 3. Classification of HEA structures: (*a*) by type of phases and (*b*) by number of phases [1]

mula $Al_xSn_yZn[CuMnNi]_{(1-xyz)}$ [30]. Alloys containing carbon, boron, or nitrogen represent a distinct group of HEAs. These elements exert a significant influence on the alloy structure, particularly the phase composition. This introduces certain challenges in alloy processing and influences the final properties. The most thoroughly investigated alloys within this group are those containing nitrogen [31–34]. Far less attention has been devoted to alloys developed according to the HEA principle involving carbon [4, 35]. In Reference [35], multicomponent coatings such as (TiZrNbHfTa)N and (TiZrNbHfTa)C deposited on a steel substrate were examined. These coatings corresponded to HEA compositions and were produced by sputtering pure metals in Ar + N_2 and Ar + CH_4 atmospheres. The coatings demonstrated excellent wear and friction resistance, with the carbon-containing coating exhibiting particularly superior performance.

Studies dedicated to the influence of boron on the properties of HEAs are relatively few. Noteworthy, contributions include [20, 36]. As reported in Ref. [20], the increasing boron content in Mo–V-based alloys reduced the thermal stability of the amorphous matrix. Additionally, a clear correlation between microhardness and boron content was identified: a decrease in hardness by approximately 30 *HV* was observed in Mo–B alloys, while V–B alloys exhibited an increase in hardness from 815 *HV* to 960 *HV* as the boron content increased.

The final group of HEAs, according to the classification proposed in Ref. [1], is based on metals such as Ag, Au, Co, Cr, Cu, Ni, Pd, Pt, Rh, and Ru. Alloys within this system are primarily intended for catalytic applications. These alloys have been investigated to a limited extent; among recent studies is [38], which focused on the development of an alloy with the composition $Cu_{30}Au_{23}Pt_{22}Pd_{25}$. This study aimed to create a porous structure, aligning with the intended catalytic application.

A principal issue in the study of HEAs and their structure concerns the phases that may form within these alloys. Ref. [1] mentions the existence of 23 distinct crystalline phases that can occur in HEAs. The most common and, consequently, the most thoroughly studied phases include solid solutions (SS), solid solutions combined with intermetallics (SS + IM), and solely intermetallic phases (IM) (Fig. 3). As illustrated in Fig. 3, the predominant phases in HEAs are disordered solid solutions with either f.c.c. or b.c.c. lattices, intermetallic phases such as Laves phases, and ordered *B*2-type intermetallic phases. Intermetallic compounds with h.c.p. structures and other electronic compounds are rare. It should be noted that the phase distribution analysis conducted in Ref. [1] revealed that the widely held belief in the predominance of single-phase structures in HEAs is a misconception. While many HEAs exhibit single-phase microstructures, a larger proportion of HEAs display two-phase structures, and multiphase structures are encountered too. Typical single-phase f.c.c. structures are represented by Cantor alloys, which are HEAs based on *d*-transition metal systems. Subsequent studies [3–4, 8, 10] have demonstrated that alloying with elements such as V, Cu, and Ti offers new opportunities for favourable phase transformations and, consequently, the potential for controlling the structure and properties of these alloys.

The methods employed for HEA production are diverse, ranging from conventional melting to the relatively rare technique of melt spinning. Common to all methods is the exclusive use of pure metals as charge materials, with melting and subsequent processing conducted in a protective atmosphere (*e.g.*, argon) to prevent oxidation. When employing conventional melting techniques, multiple remelting cycles are necessary to achieve a homogeneous structure. Further processing is utilised to ensure structural uniformity and to eliminate segregation [41, 42].

Given that many HEAs incorporate refractory metals, mechanical alloying in planetary ball mills is frequently used for alloy production. This process involves grinding pure metal powders down to nanoparticle sizes. For example, alloys within the FeCoNi*XY* system, where Cr, V, Hf, and Ti serve as the *XY* components, are produced using this approach [43].

Plasma sintering is also widely employed in HEA production. This method avoids the problems associated with powder adhesion that can occur during mechanical alloying. Plasma sintering was applied in studies [44–46] involving metal powders.

Another advanced method for HEA production is magnetron sputtering [47–49], which enables the formation of HEAs as thin films or coatings applied to substrates. Recent reviews of the current state of research on HEAs are presented in several sources [50–52].

Particularly, Ref. [50] summarises the latest developments across various material systems, with a specific focus on laser cladding of functional coatings exhibiting enhanced wear resistance, corrosion resistance, oxida-

tion stability, and improved biomedical compatibility. Based on the analysis of microstructure, mechanical properties, and corrosion resistance of HEAs and laser-cladded coatings derived from conventional alloys, it is concluded that laser cladding can significantly enhance corrosion resistance, homogenise grain size, increase microhardness, and improve other material properties.

Reference [51] provides a comprehensive overview of additive manufacturing (AM) processes employing HEAs. The review emphasises the importance of stages such as heat treatment, surface finishing, and post-processing to achieve the desired material properties and dimensional precision in components fabricated *via* AM technologies.

Reference [52] explores the structure of high-entropy solders based on *d*-transition metals, including single-phase solid solutions and eutectic structures compatible with base metals. These materials provide the necessary soldering temperature range, effective wetting performance, and favourable mechanical properties of the resulting joints. Particular attention is given to the structural evolution of solder joints using high-entropy solder, especially under conditions involving concentration gradients and interfacial diffusion, which promote the formation of high-entropy crystalline structures within the soldered zones. A brief analysis of HEA production methods and the principal trends in composition and property development leads to the following conclusions: in most cases, pure metal powders are utilised for HEA fabrication; although complex technologies such as plasma sintering and magnetron sputtering are employed, HEAs based on *d*-transition metal systems are of the greatest commercial and industrial interest; the development of HEAs within *d*-transition metal systems represents the next stage in the evolution of high-alloyed steels and alloys from the austenitic, martensitic-ageing, and DH steel classes; HEA microstructures may include various phases, such as solid solutions with f.c.c. or b.c.c. lattices, intermetallic phases including Laves phases, and electronic compounds; and the thermodynamics of HEAs complies with the Gibbs phase rule, although the observed number of phases typically reflects either the minimum possible or a quantity lower than the theoretical maximum predicted by the Gibbs rule.

3. Current Research on HEAs and Their Applications

3.1. Influence of Various Elements on the Properties of HEAs

In study [53], a high-entropy amorphous alloy $(ZrTiHfNi)_{100-x}Nb_x$ was produced *via* arc-melting and single-roller melt spinning. As the Nb content increased, the entropy of the high-entropy amorphous alloys rose gradually, thermal stability consistently improved, and the crystallisation temperature increased. The Nb20 system exhibited the highest entropy value and superior thermal stability; however, its glass-forming ability (GFA)

was weaker than that of the Nb15 system. Due to high entropy, atoms in high-entropy amorphous alloys diffuse slowly during heating, resulting in slow crystallisation kinetics and high thermal stability. Furthermore, owing to the predominance of kinetic over thermodynamic mechanisms, the amorphous-forming ability of these alloys was reduced.

The aim of the study [54] was to investigate the mechanisms by which silicon influences the phase composition, microstructure, wear resistance, and corrosion resistance of high-entropy alloy coatings. $CoCrCu_{0.5}FeNiSi_x$ (x = 0, 0.5, 1, 1.5, 2) high-entropy alloy coatings were fabricated on the surface of AISI 1045 steel using laser cladding technology. Experimental results indicated that silicon promotes the formation of silicide and b.c.c. phases. Additionally, silicon addition facilitates grain refinement and a transition from columnar to equiaxed crystals. The microhardness of the $CoCrCu_{0.5}FeNiSi_x$ coatings increased with silicon content, with the Si_2 coating reaching an average microhardness of 389.05 $HV_{0.5}$, *i.e.*, 2.33 times higher than the SiO coating (166.77 $HV_{0.5}$). As the silicon content rose, the wear resistance of the coatings improved progressively. The average coefficient of friction decreased from 0.9499 to 0.6285, while the wear rate reduced from 0.02913 mmi/(N×m) to 0.0146 mmi/(N×m). The principal wear mechanisms identified were adhesive, abrasive, and oxidative wear. Silicon addition also enhanced the corrosion resistance of the coatings.

High-entropy FeCrCoNi alloys have attracted considerable attention due to their favourable properties at ambient and low temperatures; however, their relatively low yield strength constrains broader application [55]. Few investigations have addressed high-entropy alloys with non-equiatomic ratios. The authors examined the effects of incorporating 5 wt.% titanium carbide (TiC) ceramic particles on the microstructure, mechanical properties, and tribological characteristics of $Fe_{55}Cr_{25}Co_{10}Ni_{10}$ high-entropy alloys. The addition of TiC substantially altered the alloys' phase structure, transforming it from a single f.c.c. solid solution to a composite comprising f.c.c. solid solution and TiC particles. The microstructure evolved from a uniform columnar crystal structure to a composite incorporating columnar dendrites, cellular dendrites, and unmelted TiC particles. Notably, this transformation significantly enhanced the mechanical properties: yield strength increased from 203 MPa to 254 MPa (a 25.1% improvement), while tensile strength rose from 542 MPa to 635 MPa (a 17.2% improvement).

In Reference [56], five refractory high-entropy nitride (RHEAN) coatings based on (VNbMoTaWTiAl)N with varying chemical compositions of Ti and Al were fabricated using high-power impulse magnetron sputtering (HiPIMS). The effects of varying atomic percentages of Ti and Al on the chemical composition, phase structure, microstructure, mechanical properties, and corrosion resistance of the RHEAN coatings were investigated. The study demonstrated that all coatings exhibited amorphous structures

due to the strong ion bombardment effect from the high-energy HiPIMS plasma. The crystalline structures of the coatings were disrupted and transformed into amorphous phases by the high-energy ion bombardment. Altering the input power to the TiAl target changed the film thickness, chemical composition, mechanical properties, and corrosion resistance of the coatings. The coating with Ti, Al, and N ratios of 1.2, 0.9, and 1.0, respectively, exhibited the highest hardness of 14.6 GPa and corrosion resistance 6.33 times greater than that of pure 304 stainless steel, making it a potential candidate for use in highly corrosive environments.

High-entropy alloys with the composition $FeCrMnAl_xCu$ (where x = 0, 0.1, 0.25, 0.5, 0.75, and 1.0) were synthesised using vacuum arc melting followed by casting into copper moulds [57]. The effects of varying aluminium content on the microstructure and mechanical properties of these alloys were systematically studied. The microstructural development and properties of $FeCrMnAl_xCu$ high-entropy alloys under uniaxial tension were also explored through molecular dynamics simulations. Experimental results indicated that as the aluminium content increased from 0 to 1.0, the alloys' phase structure before and after tensile testing comprised f.c.c. and b.c.c. phases. Specifically, the proportion of the b.c.c. phase increased after tensile testing, while the dendritic regions expanded and the interdendritic regions decreased. The tensile strength declined by 70.44%, and elongation decreased by 87.14% as the aluminium content increased from 0 to 1.0.

In Reference [58], high-entropy cemented carbides (HECC) (WMoNbVTa)C–Co and (WMoNbV)C–Co were developed using thermodynamic calculations, ball milling, and gas pressure sintering. Microstructural observations revealed that Ta-doped HECC exhibited finer grain size in the high-entropy carbide (HEC) matrix, fewer precipitated tungsten carbide (WC) particles, and a thinner VMo-rich segregation layer at HEC grain boundaries compared to the Ta-free counterpart. This suggests that Ta enhances the stability of both the HEC matrix and the HECC. The interfaces between the Co-rich interlayer, VMo-rich interlayer, and the HEC matrix were coherent in the Ta-doped HECC, whereas incoherent interfaces were observed in the Ta-free HECC. Consequently, the Ta-alloyed HECC demonstrated improved hardness, fracture toughness, and transverse rupture strength compared to its Ta-free equivalent.

Alloys that combine high strength and ductility with cost-effectiveness are continuously sought after for industrial applications. In study [59], a two-phase high-entropy alloy $Fe_{40}Mn_{20}Cr_{10}Ni_{20}Al_5Si_5$ (at.%) was developed, exhibiting a tensile strength of 1060 MPa and an elongation of 26%. The precipitation of a $B2$-Ni(Al,Mn) phase was utilised to strengthen the alloy, while the combination of soft and hard phases provided substantial work-hardening capability. A dual heterogeneous structure comprising partially recrystallized and precipitated phases effectively over-

came the typical strength–ductility trade-off at room temperature. For these heterogeneous structures, the rule of mixtures was applied to calculate flow stress, identifying additional strengthening contributions from dislocation hardening, dispersion hardening, and back-stress hardening.

In study [60], a detailed analysis was conducted on the evolution of the microstructure and mechanical properties of a series of high-entropy alloys (HEAs) of the $Cu_xCoCrNiAl$ system to evaluate the effect of copper content. The results indicated that as the copper content increased, the phase structure changed from f.c.c.1 + f.c.c.2 (AlCu) + b.c.c. to a single f.c.c. phase. With increasing Cu content from 20% to 80%, the alloys' hardness decreased from 515 *HV* to 135 *HV*, while the tensile strength dropped from 1335 MPa to 524 MPa. The fracture mechanism transitioned from a mixed brittle–ductile mode to a fully ductile mode. Consequently, the $Cu_4CoCrNiAl$ HEA (CA50) demonstrated superior mechanical properties, with hardness, yield strength, tensile strength, and elongation measured at 321 *HV*, 556 MPa, 846 MPa, and 16.4%, respectively.

Structural materials for fusion reactors must possess both high radiation resistance and high-temperature mechanical properties, while also satisfying low activation requirements due to nuclear waste management considerations. Study [61] examined a previously developed phase-structured HEA, $FeMnCrTi_{0.1}$, which exhibited excellent room-temperature mechanical properties surpassing those of current low-activation materials and most HEAs. This study focused on the alloys' high-temperature mechanical behaviour and radiation resistance. The alloy demonstrated a yield strength exceeding 1000 MPa and a fracture strain greater than 25% at 650 °C. It was established that the alloy possesses favourable high-temperature mechanical properties and high radiation resistance, indicating its potential for use in fusion reactors and other high-temperature, high-radiation environments.

Shape memory alloys are known to exhibit the elastocaloric effect by utilising latent heat associated with stress-induced martensitic transformation, making them suitable for solid-state refrigeration applications. In study [62], a novel boron-alloyed high-entropy shape memory alloy, $(Ti_{25}Zr_{10}Hf_{15}Ni_{25}Cu_{25})_{99.6}B_{0.4}$, was developed. This alloy leveraged the severe lattice distortion inherent to the high-entropy concept, along with boron addition to enhance mechanical properties. A large elastocaloric effect was achieved, with a maximum stress-induced temperature change of up to 17.1 K over a broad temperature range from 233 K to 473 K, surpassing the performance of most known elastocaloric materials.

The effect of titanium content on refractory high-entropy alloys (RHEAs) Ti_xVNbMo (x = 0.5, 1.0, 1.5, 2.0) was studied using both experimental and theoretical methods, focusing on phase composition, microstructure, and mechanical properties [63]. All Ti_xVNbMo RHEAs exhibited a single-phase b.c.c. solid solution structure, with the lattice parameter

increasing as the Ti content rose. Thermodynamic and kinetic stability were confirmed through analyses of formation enthalpy, cohesive energy, and phonon spectra. Increasing Ti content led to gradual reductions in hardness, yield strength, and elastic modulus, while all alloys displayed anisotropic behaviour. The Ti2.0 alloy exhibited the best ductility, whereas the Ti0.5 alloy showed the highest specific yield strength.

Study [64] explored the effect of chromium addition on the structure, microstructure, and corrosion properties of high-entropy alloys $(FeCoNi)_{0.75}Cu_{0.25-x}Cr_x$ (x = 0, 0.05, 0.1, 0.15, 0.2, 0.25), produced using vacuum arc melting. X-ray diffraction and field emission scanning electron microscopy coupled with energy-dispersive spectroscopy were employed for characterisation. Experimental results indicated that chromium significantly improved both uniform and pitting corrosion resistance. Passive current density and the passive potential range increased notably with Cr addition, reaching 0.7 μA/cm^2 and 1156 mV, respectively, at 25 at.% Cr in 1 M H_2SO_4. This improvement was attributed to the development of a more homogeneous microstructure and the elimination of microsegregation in the f.c.c. matrix, facilitating the formation of a protective chromium oxide/hydroxide layer.

The influence of nickel content on corrosion resistance was studied in Ref. [65]. Corrosion behaviour in non-equiatomic $CoCr_{0.8}FeTi_{0.4}Ni_x$ (x = 1, 2, 3, 4) HEAs was evaluated in a 3.5% NaCl solution by controlling precipitated phase amounts *via* varying Ni content. Electrochemical tests showed that $CoCr_{0.8}FeTi_{0.4}Ni_2$ exhibited the best corrosion resistance (E_{corr} = = –247 mVAg/AgCl, I_{corr} = 63.7 nA/cm^2). Corrosion mechanisms were analysed by combining elemental distribution and corrosion morphology. As Ni content decreased, the alloys' microstructure transitioned from f.c.c. + $L1_2$ phases (in $CoCr_{0.8}FeTi_{0.4}Ni_3$ and $CoCr_{0.8}FeTi_{0.4}Ni_4$) to f.c.c. + $L1_2$ + η phases (in $CoCr_{0.8}FeTi_{0.4}Ni_1$ and $CoCr_{0.8}FeTi_{0.4}Ni_2$).

In study [66], a trace amount of scandium (1 at.%) was added to a lightweight high-entropy alloy (LHEA) system composed of Al–Li–Mg–Zn–Cu. It was found that minor alloying with scandium resulted in the formation of a new strengthening precipitate phase (Al_3Sc), which effectively suppressed grain growth, reducing the average grain size of $Al_{80}Li_5Mg_5Zn_5Cu_5$ from 548.2 to 28.4 μm, significantly refining the grain structure. The addition of scandium not only improved the mechanical properties of the high-entropy alloy but also enhanced its corrosion resistance. Scandium contributed to the development of an additional passive film during the corrosion process. To optimise the properties of the $Al_{80}Li_5Mg_5Zn_5Cu_4Sc_1$ high-entropy alloy, the distribution and size of the precipitate and matrix phases were controlled through heat treatment. After ageing at 400 °C for 1 hour, the tensile and compressive strengths at room temperature increased by 68.8% and 63.4%, respectively, compared to the as-cast condition.

In study [67], the $Nb_{1-x}Mo_{25}Ta_{25}W_x$ (x = 10, 17, 25, 33, and 40) system was investigated to examine the effect of tungsten content on high-temperature creep resistance. Using molecular dynamics (MD) and Monte Carlo (MC) simulations, the creep deformation behaviour and atomic mechanisms of NbMoTaW alloys with varying tungsten content under creep loading were analysed. The results indicated that higher tungsten content enhanced the solute drag effect, thereby increasing creep resistance at elevated temperatures. Furthermore, Monte Carlo exchanges increased the tungsten content within the grains, further improving high-temperature creep resistance.

Molybdenum is a critical strengthening element in refractory high-entropy alloys (RHEAs). However, due to Mo high melting point, producing alloys with uniform elemental distribution can be challenging. In study [68], 3*D* printing, also known as laser additive manufacturing (LAM), was utilised to fabricate RHEAs in the TiZrVNbAl system with varying Mo contents. The high temperature and strong convection in the melt during the LAM process facilitated a uniform distribution of elements. As the Mo content increased, the solid–liquid temperature interval widened, promoting the formation of fine equiaxed grains and reducing the average grain size.

A nanocrystalline high-entropy alloy AlCoCrCuFeNi with 1 at.% yttrium was synthesised by mechanical alloying, and its microstructural stability was studied up to 1173 K ($0.75T_m$) [69]. Lattice parameter analysis after milling revealed a dual-phase structure, with copper and chromium identified as the host lattices for the f.c.c. (0.362 nm) and b.c.c. (0.288 nm) phases, respectively. The fraction of the f.c.c. phase was observed to increase monotonically with annealing temperature. The addition of yttrium helped stabilise the average grain size at approximately 31 nm after annealing at 1173 K and preserved 82% of the hardness (≈8.56 ± 0.3 GPa) achieved in the ball-milled base alloy.

In study [70], composites based on the high-entropy alloy ZrC/AlCoCrFeNi were produced by incorporating zirconium carbide (ZrC) into AlCoCrFeNi using spark plasma sintering. The influence of ZrC addition on microstructure, mechanical properties, and wear resistance was evaluated. The introduction of ZrC particles significantly refined the grain structure of the HEA matrix. At the ZrC content of 5 wt.%, the particles were uniformly distributed throughout the matrix. As the ZrC content increased, the coefficient of friction initially rose and then declined. The wear mechanism transitioned from adhesive and fatigue wear to abrasive and oxidative wear. Cross-sectional wear analysis showed that the oxide layer in the composite was thicker than in the HEA alone, with noticeable cavities present at the bottom of wear pits in the HEA but absent in the composite. This indicated that the addition of ZrC significantly enhanced the composite's wear resistance.

In study [71], high-entropy alloy coatings CoCrMoNb(TiC)$_x$ with varying TiC content were fabricated using laser cladding technology. The influence of TiC content on the coatings' microstructure and mechanical properties was assessed. The tribological properties of CoCrMoNb(TiC)$_{7.5\%}$ coatings were evaluated over temperatures ranging from room temperature to 800 °C. Results showed that the coatings primarily consisted of b.c.c., f.c.c., and a small amount of Laves phases. The addition of TiC introduced new compounds such as Cr_3C_2 and NbC. As the TiC content increased, the skeleton-like structure gradually bonded and fused, leading to a denser microstructure. The CoCrMoNb(TiC)$_{7.5\%}$ coating exhibited the highest microhardness of 938 $HV_{0.3}$ and excellent wear resistance ($1.6 \cdot 10^{-5}$ mm^3/(N·m)) at room temperature, attributed to a synergistic effect of solid solution strengthening, fine-grain strengthening, and dispersion strengthening by hard phases like TiC, Cr_3C_2, and NbC. This coating also demonstrated the best tribological properties at 800 °C, primarily due to the formation of a dense-glaze layer composed of Cr_2O_3, Co_3O_4, Nb_2O_5, and other oxides on the worn surface, which effectively reduced friction and enhanced wear resistance.

Eutectic high-entropy alloys (EHEAs) such as AlCoCrFeNi$_{2.1}$ show considerable potential for high-temperature applications due to their two-phase lamellar structure [72]. This study examined the high-temperature oxidation behaviour and scaling mechanisms of three EHEAs: AlCoCrFeNi$_{2.1}$ (EHEA), Y–Hf EHEA, and Pt–Y–Hf EHEA. It was observed that the oxide formed on the AlCoCrFeNi$_{2.1}$ EHEA spalled over a large surface area following short-term oxidation. Diffusion-induced voids accumulated at the oxide/alloy interface, causing spallation of the oxide under thermal stress. In contrast, the Y–Hf EHEA and Pt–Y–Hf EHEA formed continuous and adherent Al_2O_3 scales. Internal oxidation of the reactive elements Y and Hf was observed in the Y–Hf EHEA, leading to rapid growth of surrounding oxides. The addition of platinum in the Pt–Y–Hf EHEA suppressed the over-alloying effect of Y and Hf, resulting in the formation of a more homogeneous and protective a-Al_2O_3 scale.

3.2. Medium-Entropy Alloys

Medium-entropy alloys (MEAs) typically consist of three principal elements in equal atomic proportions, and their mixing entropy lies between that of conventional alloys and HEAs.

For example, the CoCrNi alloy (MEA) exhibits superior mechanical properties compared to the CoCrFeNi MEA and the CoCrFeMnNi high-entropy alloy, which possess similar microstructures, primarily due to its lower stacking fault energy [73]. Neutron diffraction results reveal significant differences in lattice strain evolution among the three alloys, with the CoCrNi MEA displaying the highest dislocation density, particu-

larly during the later stages of deformation. The more active dislocation movements in the CoCrNi MEA contribute to its enhanced ductility compared to the CoCrFeNi MEA and the CoCrFeMnNi HEA.

In study [74], strong interfacial bonding was achieved through solid solution strengthening and secondary phase reinforcement using FeCoNiCr medium-entropy alloy (MEA) particles fabricated by spark plasma sintering (SPS). Experimental results showed that the boundary layer consists of a multilayer f.c.c. solid solution and an σ-phase structure formed by the interaction between FeCoNiCr and the Ti_6Al_4V matrix, as well as microstructural features such as stacking faults and twins. The tensile strength, yield strength, and hardness of the composites improved with increasing MEA content.

In study [75], a refractory medium-entropy alloy based on Ta–W reinforced with carbide was fabricated by spark plasma sintering. It was demonstrated that the alloy possesses high compressive ductility at room temperature and exhibits high strength at elevated temperatures. The microstructure of this alloy consists of a b.c.c. matrix with M_2C carbides, within which nanoscale HfO_2 particles are dispersed. The M_2C carbides have a micron-scale size, with metallic matrix interlayers situated between them. The presence of carbides significantly enhances the high-temperature strength of the alloy, resulting in yield strength of 352 MPa and a compressive strength of 426 MPa at 1750 °C.

Study [76] investigated the effect of grain size on the corrosion resistance of TiZrNb medium-entropy alloys (MEAs) in physiological saline solution (0.9 wt.% NaCl solution). The results indicate that the corrosion resistance of TiZrNb decreases as the grain size decreases. This deterioration in corrosion resistance can be attributed to the synergistic effect between defect accumulation and grain refinement caused by surface mechanical attrition treatment (SMAT).

Study [77] focused on the development of a low-friction coating material using a ternary medium-entropy alloy comprising lead (Pb), tin (Sn), and copper (Cu). The alloy investigated in this study was fabricated by induction melting. It was found that stable Pb–Sn phases enriched with Pb and Cu–Sn phases formed. The average microhardness was 25.3 ± 13.61 *HV*, which is suitable for coating applications. Corrosion tests conducted in a 3.5 wt.% NaCl environment revealed the formation of a stable passive layer.

3.3. Design of HEAs

Study [78] presents a method for adjusting cross-scale heterostructures in HEAs and provides design recommendations for CoCrNi-based HEAs with high strength, high ductility, and excellent antioxidant properties. High-entropy alloys with a single-phase f.c.c. structure are widely used as structural materials due to their excellent plasticity and ductility. However,

the strength and oxidation resistance of single-phase f.c.c. alloys remain insufficient. Conventional methods for increasing strength often reduce ductility, making them unsuitable for practical use. This study proposes a strategy for preparing $Al_xCoCr_{0.6}NiV_{0.6}$ alloys based on CoCrNi, characterised by unequal atomic ratios and high entropy, incorporating aluminium and vanadium. In each alloy composition, short-range order was observed, varying in size and crystal plane families. At the aluminium content of x = 0.85, both f.c.c. and b.c.c. dual phases were present in the alloy. The heterogeneous structure and presence of dual phases significantly enhanced the strength and oxidation resistance of the HEA at high temperatures. The yield strength of the HEA increased from 235 MPa to 974 MPa, while the oxide layer thickness decreased from 37.5 to 8.3 μm, representing a reduction of 77%.

In study [79], various thermodynamic parameters were calculated, and their dependencies on the content of alloying elements were established. The alloying limits of the experimental alloys were determined in accordance with the criteria defined for high-entropy alloys (HEAs). Melting temperatures were calculated, and the liquidus domain of the NiCoCrAl–(Ti,Nb) system was delineated.

In study [80], the temperature dependence of the propagation velocity and attenuation of plane-polarised ultrasonic waves at a frequency of 50 MHz in the high-entropy alloy $Al_{0.5}CoCrCuFeNi$ was investigated using ultrasonic spectroscopy over the temperature range of 77–300 K. The anisotropy of the alloys' acoustic properties was found to be attributable to growth texture. A significant level of ultrasonic wave attenuation was also observed.

In study [81], theoretical guidelines are proposed for the design of high-performance lightweight refractory high entropy alloys. The occupation of oxygen atoms in interstitial sites within HEAs demonstrates site preferences, thereby affecting the alloy properties. First-principles calculations were used to investigate the physical origins of local site preferences for oxygen in the HEA $Ti_3Zr_{1.5}NbVAl_{0.25}$. The results show that formation energies are closely correlated with the coordinating atoms in the interstitial environment. Interstitial oxygen tends to occupy coordination environments rich in Ti and Zr, which does not favour the stabilisation of Al coordination environments. This local site preference primarily depends on the amount of charge transfer and lattice distortion, which drives interstitial oxygen to occupy Ti- and Zr-rich environments. Conversely, minimal charge transfer between Al and oxygen hinders the solid solution of interstitial oxygen.

The use of multiple elements in alloying offers promising opportunities for developing new alloys from multicomponent scrap and electronic waste, reducing dependence on critical metals and highlighting the need for advanced data generation methods. Given the vast potential offered by

this multicomponent raw material, modelling and AI-based tools are essential for efficiently exploring and optimising new alloys, supporting sustainable progress in metallurgy [82]. These advances require a reimagined alloy design framework, emphasising reliable data acquisition, alternative design parameters, and advanced computational tools compared to traditional composition-focused methodologies.

Partially recrystallized precipitation-strengthened HEAs have demonstrated high mechanical properties with yield strengths up to 2 GPa. However, the recrystallization kinetics of precipitation-strengthened HEAs is not well understood due to the complex interactions between precipitation and recrystallization. The authors [83] report anomalous recrystallization behaviour in precipitation-strengthened HEAs, where the recrystallization kinetics at 600 °C is faster than at 800 °C. Moreover, the recrystallization period at 800 °C is significantly shorter than at 600 °C. Through comparative analysis, the anomalous recrystallization kinetics were attributed to a delayed pinning effect caused by slow precipitation kinetics at 600 °C, while the shortened recrystallization period at 800 °C was due to a high nucleation rate of recrystallization through particle-stimulated nucleation.

The growing demand for lightweight, high-performance materials in modern structural applications drives research into developing new alloys with low density and high entropy, as well as shape memory alloys. Study [84] focuses on the development and characterisation of a non-equiatomic, low-density, multiphase alloy $(Ti_6Al_4V)_{50}(Ni + Co)_{50}$. The alloy exhibits an improved microstructure, significantly reduced density of approximately 5.2 g/cm^3 (lower than conventional Ni-based shape memory alloys and other low-density HEAs) and excellent mechanical properties, including high compressive yield strength.

Study [85] examines as-cast, homogenised, and aged states with precipitation properties of alloys $Co_xCr_xFe_xNi_{60-2x}V_{40-x}$ in a low-entropy alloy (x = 1, 2, and 5) and a high-entropy alloy (x = 10, 15, and 20). After solution treatment, the phase stability of the six alloys was individually compared, and the formation of σ-phase was comprehensively calculated and predicted using valence electron concentration (VEC) parameters and paired σ-phase forming elements (PSFE), resulting in a structure containing both f.c.c. and σ-phases. As vanadium content increased beyond the solid solution criteria in the high-entropy alloys, the homogenised and aged states precipitated σ-phases. It was observed that for low-entropy alloys, the activation energy increased with rising configurational entropy. Conversely, for high-entropy alloys, the influence of entropy decreased, while the effect of sluggish diffusion became more pronounced.

In study [86], a framework for material design combining solid solution strengthening with machine learning (ML) was proposed. The framework integrates two approaches: (1) a machine learning method using

Gaussian process regression (GPR) with forward/backward selection and Yeo–Johnson transformation, and (2) a heuristic approach employing symbolic transformation (ST) to derive interpretable descriptors. SHapley Additive exPlanations (SHAP) analysis identified activation energy barriers, mixing entropy, and volume mismatch as critical physical characteristics. The ST algorithm further highlighted a three-term descriptor: an enthalpy element, a heavy element mass component, and a correction factor, achieving a Pearson correlation of 0.86. Based on the solution proposed by the constructed Gaussian regression model, five compositions in the ZrTiNbTaV system were fabricated, and their microstructure and mechanical properties were tested. The model demonstrated reliable generalisation for various HEA systems, showing <15% deviation in yield strength predictions.

In study [87], the behaviour of HEAs and single-layer graphene-adsorbed high-entropy alloys (Gr/HEA) during nanoscratching was investigated using molecular dynamics modelling. Analysis of surface morphology, tribological properties, and stress distribution revealed a significant influence of the graphene layer on the tribological behaviour of HEAs during scratching. The results showed that the HEA exhibited stronger surface plastic deformation, higher transverse force (F_x), lower normal force (F_z), and a higher coefficient of friction compared to Gr/HEA. Additionally, the stress distribution region in the HEA was significantly larger, with higher stress concentration. The graphene layer effectively enhanced the tribological properties of the HEA through lubrication mechanisms, stress damping, and load distribution. This study provides a theoretical basis for applying graphene as a surface modification layer for HEAs.

Study [88] demonstrates the feasibility of developing multicomponent high-entropy filler materials for brazing based on the NiCoCrPdGe system. This was achieved using computational methods, binary phase diagrams, and classical Hume-Rothery rules for solid solution formation.

Study [89] utilised molecular dynamics modelling to investigate the femtosecond laser ablation process of the CrCoFeMnNi HEA, focusing on changes in internal microstructure, temperature, stress, and mechanical properties. The results showed that increasing the laser energy density led to a substantial rise in both temperature and stress within the lattice structure. At a fixed pulse width, higher laser energy densities correlated with elevated lattice temperatures and accelerated cooling rates, highlighting the pronounced impact of laser energy on thermal dynamics. In contrast, the effect of pulse width on temperature relaxation time was comparatively minimal. When the temperature at the laser focus exceeded 5000 K, the morphology of the high-temperature region aligned with the laser beam, demonstrating that femtosecond lasers exhibited minimal thermodiffusion effects.

In study [90], first-principles calculations were used to investigate the maximum hydrogen storage capacity of two HEAs: VNbTaTi and VNbTaTiAl. Based on the binding energy calculations of the high-entropy hydrides, it was found that hydrogen atoms predominantly occupied octahedral interstitial sites in b.c.c. structures and tetrahedral interstitial sites in f.c.c. structures. The VNbTaTi and VNbTaTiAl hydrides, both initially b.c.c., transformed into f.c.c. structures at hydrogen-to-metal ratios (H/*Me*) of 1.17 and 1.27, respectively. As the hydrogen content increased, the stability of the b.c.c. hydride decreased, while the stability of the f.c.c. hydride increased. Radial distribution function calculations indicated that, after the phase transition, hydrogen atoms in both hydrides were more orderly arranged. The thermodynamic and dynamic stability of the two HEA hydrides was assessed. Results indicated that VNbTaTiAl had a higher maximum hydrogen storage capacity (2.46 wt.%) than VNbTaTi (2.01–2.12 wt.%), highlighting its potential for hydrogen storage applications.

Rapid melt quenching to produce metastable or amorphous phases is a promising method for developing new high-strength and corrosion-resistant HEA materials [91]. In the present study, the effect of rapid quenching on the phase formation process of the Zr–Al–Ni–Co–Cu HEA was investigated. Samples of the $Zr_{40}Al_{20}Ni_5Co_{15}Cu_{20}$ alloy were produced using conventional arc melting under an argon protective atmosphere. Rapidly quenched samples in the form of cylindrical rods with a diameter of 3 mm were obtained from the alloy ingots by vacuum casting into a copper mould. The structure of the ingots and rods was examined using x-ray diffraction and scanning electron microscopy, and their heating behaviour was studied by differential scanning calorimetry. It was shown that the rapidly quenched alloy predominantly comprised the Laves phase ZrCoAl, a $Cu_{0.6}ZrCo_{0.4}$ solid solution, and the ZrNiAl phase. An exothermic reaction in the rapidly quenched sample occurred at 960–980 K. The Kissinger method was used to calculate the activation energy of the detected reaction. Rapid quenching significantly refined the grains of the Laves phase, increased stability, and boosted the volume fraction of the solid solution. The obtained results could be applied to further practical use of rapidly quenched HEAs.

Material property studies based on atomic structure are a widely used approach. However, when studying complex systems such as HEAs, atomic structure not only encompasses an overly vast chemical space but also has imprecise correlations with chemical properties. The authors [92] propose a machine-learning model based on spectroscopic descriptors to study the catalytic properties of AgAuCuPdPt HEA catalysts. Even if the atomic structures of two such alloys differ, they may exhibit similar catalytic properties if their spectral characteristics coincide. This model can be extended to other systems with similar outcomes. It not only highlights the potential of spectral analysis for identifying high-performance alloy cata-

lysts but also contributes to the development of a new spectrum-based modelling approach and theoretical framework in materials science. Cluster analysis of CO spectra adsorbed on AgAuCuPdPt HEAs, combined with the catalytic properties of each cluster, revealed a group of HEAs with high selectivity towards C_2^+ products.

Study [93] compares the microstructure and mechanical properties of the $Al_{0.3}CoCrFeNiTi_{0.15}$ HEA fabricated using additive manufacturing processes, namely, direct energy deposition (DED) and selective laser melting (SLM). The results showed that the DED-produced alloy exhibited large grains, predominantly columnar with central equiaxed grains. Mechanical property tests revealed that the DED-fabricated sample achieved a tensile strength of 930.1 ± 19.3 MPa and ductility of 10.9 ± 1.6%, while the SLM-fabricated sample demonstrated a tensile strength of 979.6 ± 26.7 MPa and ductility of 30.3 ± 2.1%. The SLM process demonstrated superior overall performance in fabricating the $Al_{0.3}CoCrFeNiTi_{0.15}$ HEA.

Study [94] reports the production of a solid AlTiVCr HEA using self-propagating high-temperature synthesis (SHS) in the Cr_2O_3–V_2O_5–TiO_2–Al system. To reduce production costs, various grades of Cr_2O_3 were used as raw materials. Results showed that the alloy consisted of a solid solution phase with a b.c.c. crystalline structure, while Al_2O_3 was the primary phase in the slag. Microstructural analysis confirmed the development of an intermediate Ti_3Al phase in alloys produced with laboratory-grade Cr_2O_3. The hardness and density of the produced alloy ranged from 608 *HV* to 863 *HV* and 4660 to 5059 kg/m^3, respectively. These results confirmed that SHS is a simple method for producing lightweight AlTiVCr alloys with high hardness.

A brazed joint of high-entropy carbide (HfZrTiTaNb)C (HEC) bonded with a simple CoCrFeNi HEA was studied at 1440–1550 °C [95]. At these temperatures, HEC grains dissociated into the liquid alloy, and self-diffused Zr atoms at the grain boundary between HEC and the liquid alloy led to the formation of a Zr-enriched HEC phase (ZHEC) attached to HEC grains. The ZHEC phases were characterised by increased Zr content up to 21.44 at.% and coherent orientation with the HEC. The CoCrFeNi alloy did not undergo phase separation after solidification. A joint strength of 266 MPa was achieved when brazed at 1460 °C. At a testing temperature of 1000 °C, the joint strength remained at 87 MPa, indicating its potential for high-temperature applications. Intergranular fracture of the CoCrFeNi alloy at elevated temperatures was the cause of the reduced joint strength.

In study [96], a new approach to the development of eutectic high-entropy alloys (EHEAs) combining high strength and high ductility was considered. These alloys were designed using a combination of methods, including thermodynamic modelling and practical experiments. Additionally, improvements in the mechanical characteristics of EHEAs were achieved by creating a composite microstructure. This microstructure encompasses

a eutectic structure with a solid solution phase of either f.c.c. or b.c.c. type, as well as intermetallic or bimodal eutectics consisting of two distinct eutectic structures.

High entropy alloys (HEAs) of the $CuCrCoFeNi_xTi$ system (x = 0, 0.5, 1, 1.5, 2.0) were developed [97]. As the Ni content increased, the density of the HEA increased, the lattice constant decreased, and Poisson's ratio increased, indicating that the fracture mode of the HEAs shifted from brittle to ductile. Density of states diagrams showed that $CuCrCoFeNi_2Ti$ had the highest density. Finally, $CuCrCoFeNi_xTi$ HEAs were prepared by vacuum arc melting followed by homogenisation. As the Ni content increased, the microstructures of the HEAs became more homogeneous, the compressive strength increased from 710.3 to 1878.5 MPa, and the elongation increased from 4.9 to 14.7%. The fracture morphology of the $CuCrCoFeNi_xTi$ HEAs exhibited quasi-cleavage, primarily manifested as cleavage steps.

Additively manufactured (AM) HEAs exhibit high yield strength and significant tensile ductility [98]. A eutectic HEA (EHEA) $AlCoCrFeNi_{2.1}$ was fabricated using laser powder bed fusion (L-PBF) in as-printed form (EHEA1) and subsequently annealed at 1000 °C (EHEA2) and 600 °C (EHEA3) to achieve a wide range of mechanical properties. The recrystallized EHEAs retained their original mechanical properties, with EHEA3 being 47% harder than EHEA2, largely due to the higher $B2$-phase content and the preservation of the nanolamellar morphology.

The HEA $Fe_{20}Co_{20}Ni_{40}Al_{20}$ exhibits a dual-phase structure consisting of b.c.c. and face-centred cubic (f.c.c.) crystals. Study [99] examines the effects of deep cryogenic treatment (DCT) at –196 °C for durations ranging from 0 to 48 hours on $Fe_{20}Co_{20}Ni_{40}Al_{20}$ HEA synthesised by vacuum induction melting. The microstructure, mechanical properties, and fracture behaviour of the alloy were thoroughly analysed. The results showed that dislocations formed and migrated during DCT, creating dislocation tangles. After 36 hours of DCT, the Vickers hardness increased by 13.3%, reaching 461.5 *HV*. Additionally, the tensile strength improved by 31.4%, reaching 886.2 MPa, while elongation increased by 129% to 6.70% compared to the untreated sample. These improvements were attributed to multiple strengthening mechanisms, including grain refinement, dislocation strengthening, strengthening from nanosize dislocation cell structures, and second-phase strengthening. This study confirms that DCT is an effective method for improving the mechanical properties of $Fe_{20}Co_{20}Ni_{40}Al_{20}$ HEA.

Refractory HEAs with exceptionally high-temperature mechanical properties are attracting increasing interest in aerospace applications. However, the presence of multiple principal alloying elements poses challenges in selecting a suitable and cost-effective alloy for specific applications. A multi-property composition design method combining machine learning and thermodynamic calculations was proposed. Out of several

hundred thousand candidates, three TiZrHfNbVMoTa alloys were selected [100]. These alloys exhibited enhanced synergy between compressive strength and ductility, achieving fracture strains exceeding 60% and a yield strength of 1051 ± 23 MPa at room temperature.

Several studies have also examined the use of HEAs as coatings. Article [101] describes the defects that may be caused by laser cladding of HEA coatings, discusses various optimisation methods, and summarises the optimisation process. This article provides an in-depth analysis and summary of these aspects for the first time and investigates process optimisation measures in terms of processing parameters, material properties, and thermal treatment.

Laser cladding [102] was used to fabricate coatings of the $AlCoCrFeNiTiWC_x$ HEA (x = 0, 0.5, 1, 1.5, 2) reinforced with μ-phase and in-situ (Ti, W)C carbides. The effect of carbon content on the microstructure, microhardness, and wear resistance of the coatings was investigated. The results showed that all coatings exhibited a dominant b.c.c. phase. As the carbon content increased, the μ-phase evolved from a blocky to a network structure, while its volume fraction decreased. Simultaneously, the carbides transformed from nearly spherical to flower-shaped and dendritic morphologies, with their volume fraction increasing. Wear resistance initially improved and then decreased, with the C_1 coating showing the highest resistance.

Tribocorrosion has long been a challenge in marine environmental protection. To address this issue, study [103] employed in-situ laser cladding synthesis to fabricate composite coatings of CrMnFeCoNi HEA containing multiple ceramic reinforcing phases. By analysing the microstructure, microhardness, electrochemical properties, and tribocorrosion performance of the cladding layer, the influence of different B_4C and Ti mixture additions (10%, 20%, and 30%) on the composite coatings was examined. The results showed that the synergistic effect of carbides and borides significantly enhanced the passive surface capability of the composite material. The C_{20} coating with 20% addition exhibited the best corrosion resistance. The deposition of TiC particles not only suppressed dislocation movement but also effectively blocked corrosion development. At 30% mixture addition, the C_{30} coating achieved the highest microhardness of 380.35 $HV_{0.2}$, demonstrating optimal tribocorrosion resistance.

Dissimilar laser joining of AA6061 aluminium alloy and low-carbon steel was performed using a porous FeCoCrNi HEA coating [104]. At low laser power, the interfacial reaction zone mainly consisted of η-Zn solid solution, eutectoid Zn–Al structure, and extremely thin AlNi. Due to poor wettability of the filler metal on the steel substrate, the joint strength was low (218.3 N/mm), and the fracture mode was brittle. At high laser power, the η-Zn solid solution decreased, and AlNi thickened. Improved wettability enhanced the joint strength. The maximum joint strength of 297

N/mm was achieved at a laser power of 3000 W. The fracture mode was a mixture of brittle and ductile fractures.

Study [105] proposes a novel approach for producing a high-entropy alloy based on the Cantor system using wire arc additive manufacturing (WAAM) with a metal powder-filled cored wire.

Study [106] reported the characteristics of a cobalt-free, two-phase $FeCrNiMoSi_x$ coating as a function of silicon content. It was found that the $FeCrNiMoSi_{0.5}$ coating exhibited optimal corrosion resistance, attributed to the synergistic effect of the two-phase structure. Hardness increased with silicon addition, but wear resistance remained unchanged.

In study [107], a microarc oxidation (MAO) coating method was proposed for the surface of the AlCoCrFeNi HEA. By regulating the sintering temperature of the HEA, a high-performance HEA-based MAO coating was successfully produced. Wear and corrosion resistance of the coating were evaluated using friction testing and electrochemical corrosion testing. The results showed that the coating mainly consisted of Al_2O_3 with small amounts of Co, Fe, and Ni oxides on the surface, among which Co_3O_4 was the primary cause of the blue spots observed. Compared to the HEA7 sample, the HEA7-M coating was thicker, had a lower coefficient of friction, higher hardness, and demonstrated excellent wear resistance and significantly improved corrosion resistance.

3.4. Effect of Microstructure on the Mechanical and Physical Properties of HEAs

The study [108] presents the results of an investigation into the structure and properties of high-entropy cermets of the Ti–Cr–Fe–Ni–C system, synthesised from a precursor mixture comprising ferrotitanium, high-carbon ferrochrome, and nickel powders using powder metallurgy (hot forging of powder compacts) and arc melting techniques. According to the x-ray diffraction analysis, the alloys' phase composition includes two disordered solid solutions with predominantly f.c.c. and b.c.c. structures, as well as carbide phases: cubic MC (in hot-forged specimens) and M_7C_{33} (in specimens obtained by arc melting). A substantial difference in the microstructural features of the alloys fabricated *via* the two processing routes was demonstrated.

Study [109] investigated the correlation between the microstructure, mechanical, and magnetic properties of the high-entropy alloy $FeCoNiAl_{0.75}Nb_{0.25}$. The results showed that the alloys' microstructure included a b.c.c. solid solution phase along with a eutectic mixture of f.c.c. phases and intermetallics. Thermal treatment led to significant microstructural evolution. The precipitation of needle-like intermetallic phases occurred rapidly with increasing annealing temperature, peaking at 825 °C before decreasing markedly at 1000 °C. Consequently, the alloys' hardness

and compressive yield strength increased rapidly, reaching maximum values of approximately 600 *HV* and 2000 MPa, respectively. However, precipitation negatively affected the magnetic properties. The best values in the as-cast condition for saturation magnetisation and coercive force were 0.67 T and 716 A/m, respectively, while the hardness remained at 493 *HV*. Therefore, this alloy is highly suitable for magnetic components requiring superior mechanical performance.

Authors of Ref. [110] report on the microstructure and mechanical properties of $Al_{0.4}Cr_{0.7}FeNi_2V_{0.2}$ alloy after cold rolling, recrystallization, and ageing at 600 °C for varying durations. The results revealed that the b.c.c. solid phase formed in all aged alloy samples, while the $L1_2$ phase was detected only in the alloy aged for 48 and 96 hours. The precipitation of $L1_2$ and b.c.c. phases enhanced the alloys' hardness. Over extended ageing periods, the grain size initially decreased and then increased, with the b.c.c. phase gradually coarsening. As a result, the alloy aged for 48 hours demonstrated the best properties, with a tensile strength of 1514 MPa and an elongation of 23%. These findings clarify the effects of grain size and precipitate type on the mechanical properties of the alloy.

In study [111], the evolution of structure and phase composition in cast multicomponent alloys based on the MnFeCoNiCu system was examined in relation to variations in mixing enthalpy and entropy, atomic size difference, and valence electron concentration, starting from a medium-entropy TiFeCoNi alloy and progressing towards a Cantor-like composition. The findings revealed a transformation in crystal structure from f.c.c. to b.c.c., along with changes in phase composition. These structural modifications were shown to result in substantial strengthening while retaining ductility.

Using an ultrasonic ball mill (USBM), ultrafine powders (UFPs) of the AlCoCrCuFeNi system were produced from coarse-grained powder mixtures (CGPMs) of aluminium, iron, cobalt, copper, nickel, and chromium. Study [112] investigated the influence of copper content on the phase composition and magnetic properties of the resulting powders.

The f.c.c.-structured high-entropy alloys (HEAs) exhibit exceptional strain-hardening capabilities under both ambient and cryogenic conditions due to deformation mechanisms such as twinning and stacking faults. Study [113] examined the microstructure and mechanical properties of $Al_{0.25}CoCrFeNi$. As the grain size decreased, the yield strength at both 25 °C and –196 °C increased due to grain boundary strengthening. At 25 °C, the deformation mechanism transitioned from dislocation slip to deformation twinning as the grain size increased. At –196 °C, deformation twins were observed in fine-grained samples, with their density increasing and spacing decreasing as the grain size grew.

In the f.c.c. HEA CrCoNi, dislocation dissociation, nanotwinning, and transformation-induced plasticity are enhanced at cryogenic temperatures

(<77 K) [114]. In the b.c.c. HEA $Nb_{45}Ta_{25}Ti_{15}Hf_{15}$, screw dislocations, twinning, and shear band formation are activated at temperatures ranging from 77 K to 1473 K. These deformation mechanisms impart exceptional fracture resistance in both CrCoNi and $Nb_{45}Ta_{25}Ti_{15}Hf_{15}$. However, their stress-strain behaviours differ significantly at these temperatures; while CrCoNi exhibits extensive strain hardening, $Nb_{45}Ta_{25}Ti_{15}Hf_{15}$ shows nearly elastic, perfectly plastic stress-strain behaviour.

The f.c.c.-HEAs demonstrate generally a high ductility and are expected to be used in cryogenic engineering [115]. However, their moderate yield strength at cryogenic temperatures (typically below 1 GPa) and high cost limit their applications. It was determined that the Fe-based HEA $(Fe_{62}Ni_{16}Co_9Mn_9Ti_4)_{97}Si_3$ possesses high cryogenic tensile strength (yield strength and tensile strength of 1325 and 1446 MPa, respectively) and ductility (uniform elongation of 20%).

Study [116] investigated the microstructure and mechanical properties of two novel non-equiatomic HEAs, produced at two different average cooling rates (≈1000 and ≈250 K/s for samples with diameters of 2 mm and 4 mm, respectively): $Zr_{27.5}Hf_{11.1}Ti_{6.2}Cu_{32.4}Ni_{10.7}Co_{5.5}Al_{6.6}$ and $Zr_{29.7}Hf_{16.8}Ti_{5.2}Cu_{6.3}Ni_{12.1}Co_{8.4}Al_{21.5}$ (at.%). For each cast sample, the cooling rate also varied with distance from the centre (lowest) to the edge (highest), enabling the study of microstructural evolution across a wide range of cooling rates. For the composition of $Zr_{27.5}Hf_{11.1}Ti_{6.2}Cu_{32.4}Ni_{10.7}Co_{5.5}Al_{6.6}$, variations in mechanical properties between the most and least cooled regions from a narrow edge amorphous ring (nanoindentation hardness $H = 8.2 \pm 0.42$ GPa) to the centre of the largest sample ($H = 8.2 \pm 0.35$ GPa) were minimal. This was attributed to slight microstructural differences, mainly the formation of a b.c.c. solid solution phase with some h.c.p. phase. For $Zr_{29.7}Hf_{16.8}Ti_{5.2}Cu_{6.3}Ni_{12.1}Co_{8.4}Al_{21.5}$, more substantial microstructural and mechanical property differences were observed between the most and least cooled regions.

The study examined microstructural changes and mechanical properties of the $Fe_{37}Ni_{36}Al_{17}Cr_{10}$ alloy at 600 °C over a one-year testing period [117]. This dual-phase alloy can be utilised in nuclear power applications at varying temperatures. During exposure, the overall microstructure remained unchanged. The alloys' mechanical properties remained stable without significant degradation in service performance.

Study [118] investigated the microstructure, mechanical, and corrosion behaviour of high-entropy alloys (HEAs) $AlFeNiMnCu_x$ ($x = 0.5$, 0.75, 1.0, 1.25). The alloy was identified as a b.c.c. solid solution. Increasing Cu concentration promoted the formation of reinforcing phases and enhanced solid solution strengthening, improving mechanical properties. Additionally, Cu inclusion led to the formation of f.c.c. structures, facilitating the transformation of corrosion modes and thus suppressing corrosion. Among the studied HEAs, AlFeNiMnCu ($x = 1.0$) was particularly notable for its mechanical properties, exhibiting yield strength of 1559 MPa, frac-

ture strength of 1699 MPa, plastic strain of 14.3%, and a Vickers hardness of 563 *HV*.

The structural and phase state of the high-entropy alloy CoCrFeNi, formed by laser alloying of commercially pure iron surface layers with a powder mixture of pure Co, Ni, and Cr elements in equiatomic proportions, was investigated using x-ray diffraction, electron probe microanalysis, and metallographic examination. As shown in study [119], the formation of a multicomponent substitutional solid solution with a face-centred cubic (f.c.c.) lattice (typical for high-entropy alloys) occurred within the surface layers during the laser alloying process. The influence of the atmospheric environment during alloying on the structure formation processes and phase composition of the modified surfaces was also analysed.

For the first time, ultrafine powders (UFPs) of high-entropy alloys (HEAs) in the AlCoCrCuFeNi system were obtained by ultrasonic milling of a coarse-grained powder mixture of aluminium, iron, cobalt, copper, nickel, and chromium in a ball mill. X-ray diffraction, Мцssbauer spectroscopy, and magnetic measurements revealed that the phase composition and magnetic properties of the UFPs were significantly influenced by the aluminium and chromium content [120].

Study [121] explores the development of high-entropy shape memory alloys (HE-SMAs). The authors emphasise that these novel HE-SMAs may offer a promising solution to the fatigue-related limitations of conventional shape memory alloys, owing to their distinctive structure, which provides superior resistance to irreversible plastic deformation.

In Reference [122], MD simulations were used to study the influence of structure and plasticity on the tensile deformation of the HEA $Co_{25}Ni_{25}Fe_{25}Al_{7.5}Cu_{17.5}$. The results indicated that the alloys' strength increased from 1.5 to 2.2 GPa. As the coarse-grain diameter (D_{sp}) increased, the volume fraction of f.c.c. to b.c.c. phase transformation also increased, advancing the phase transformation. This transformation predominantly occurred in coarse-grained areas, where the high hardness of the b.c.c. phase was mechanically incompatible with the surrounding soft-grained areas, leading to a strengthening mechanism induced by heterogeneous deformation (HDI).

4. Quasi-HEAs

It should be noted that a common disadvantage of all the high-entropy alloys (HEAs) discussed above is their high cost compared to traditional materials. This is attributed to the feedstock, as HEAs are produced from pure metals, as well as the specific features of the melting process, which often involves mandatory remelting, rapid solidification, and other methods aimed at improving structural homogeneity.

To address these issues, the development of so-called quasi-high-entropy alloys (QHEAs) has become an increasingly popular area of research.

The general principle of QHEA design is similar to that of HEAs: a multicomponent system comprising at least five elements is used. However, strict adherence to equiatomic concentration is not required, and the feedstock and melting process requirements for QHEAs are significantly less stringent. This allows for enhanced commercial viability of QHEAs while maintaining properties comparable to those of HEAs.

Studies [123–126] investigated the feasibility of producing QHEAs based on the CoCrFeMnNi system with the partial use of ferroalloys, which significantly reduces alloy costs.

The following feedstock materials were employed for melting: ferromanganese grade FeMn80C05 (GOST 4755-91), ferrochrome grade FX001A (GOST 4757-91), metallic nickel grade N-1u (GOST 849-97), and metallic cobalt grade K1Au (GOST 123-2008). The chemical composition of the feedstock materials is presented in Table 1. The primary element contents were determined using a Niton spectrometer, while the values for other elements were provided in accordance with the respective standards.

The feedstock composition was selected so that the proportion of each component in the final alloy was approximately 20%.

The particle size distribution of all components consisted of 90% fractions within the range of 3–5 mm. The feedstock mixture was thoroughly blended and melted in a laboratory furnace model UIP-16-10-0.005(Fe)-UHL4, equipped with an enhanced cooling system. To achieve compositional uniformity and prevent external contamination, the resulting ingot (mass 0.9 kg) was poured into a chemically inert KMC crucible, remelted, and then poured again into a KMC crucible. After complete cooling, samples were prepared from the ingot for analysis. Chemical composition, microhardness, strength, and microstructure were examined.

The chemical composition of the experimental ingot was determined using a Poly Spec-F spectrometer. Fine structural analysis of the experimental samples was conducted using a TESCAN VEGA scanning electron microscope equipped with an energy-dispersive x-ray spectrometer.

X-ray diffraction studies were carried out using an X'PertPRO diffractometer with CuK_α radiation. The experimental spectra were processed using the diffractometer software packages: X'Pert High Score Plus version 2.2b and X'Pert High Score version 2.2b.

Microhardness measurements were conducted using a Willson 1150 instrument, with no fewer than five measurement points. Ultimate strength was determined using an INSTRON testing machine, with three replicates performed.

Table 2 presents the results of the chemical analysis of the experimental ingot.

A comparison alloy was produced by vacuum arc melting of pure metals, followed by casting into a water-cooled copper mould. To ensure chemical homogeneity, the ingot was remelted at least five times.

As shown in Table 2, the composition of the experimental alloy does not correspond to an equiatomic ratio, although it can still be classified as a quasi-high-entropy alloy, as the concentration of each element does not exceed 35% but is greater than 5%.

The relatively low Fe content in the experimental alloy is attributed to its low concentration in the ferromanganese used (FeMn80C05 grade). The use of ferromanganese with a higher iron content was not considered, as such grades typically contain a high carbon content (around 7%), which was undesirable in this study.

Table 3 presents the results of the microhardness and strength tests.

The data in Table 3 indicate that the experimental alloy is not inferior to the comparison sample in the specified characteristics.

Table 1. **Chemical composition of feedstock materials according to GOST [126]**

Element, % Material	Mn	Fe	Cr	Ni	Co	C	Si	P	S
FeMn80C05	75.1	25.2	—	—	—	≤0.1	1.85	≤0.3	≤0.03
ФХ001А	—	32.04	68.2	—	—	≤0.01	0.82	≤0.02	≤0.02
Ni H-1*y*	—	—	—	99.95		≤0.01	0.002	0.001	0.001
Co K1A*y*	0.03	0.2	—	—	99.3	0.02		0.003	0.004

Table 2. **Chemical composition of the resulting ingot [126]**

No.	Element, %	Fe	Cr	Mn	Co	Ni	Si + others
1	Experimental	15.3	23.3	22.4	19.1	19.2	0.70
2	Comparison	20.06	19.87	19.46	19.87	19.97	0.77

Table 3. **Results of microhardness and strength investigations [126]**

Sample	Microhardness, *HV*	Tensile strength, MPa	Average grain size, μm
Experimental	130	430	183
Alloy to be compared	136	443	180

Table 4. **Concentrations of chemical elements (wt.%) [123]**

Spectrum	Element content in the selected spectrum, wt.%					
	Ni	Cr	Fe	Mn	Co	Si
1	18.9	23.1	15.3	21.43	18.9	—
2	19.32	23.2	14.87	22.13	19.21	—
3	19.21	22.98	15.02	22.31	19.5	—
4	19.28	22.30	15.2	22.48	19.6	—
5	—	—	—	—	—	0.9

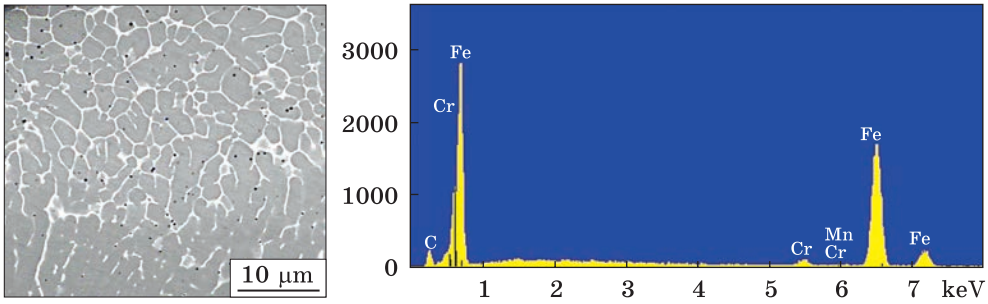

Fig. 4. Microstructure of the experimental alloy (left) and its characteristic spectrum (right) [126]

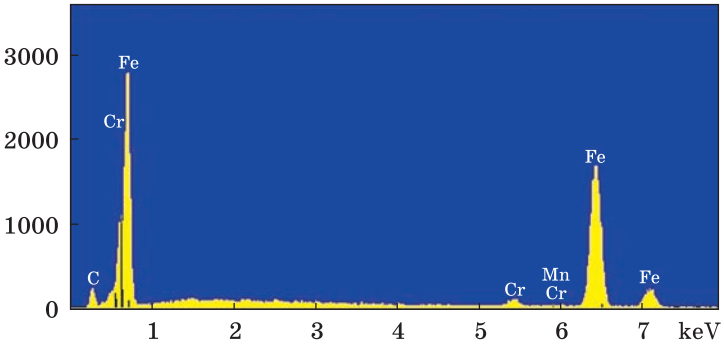

Fig. 5. Characteristic spectrum of an inclusion [123]

Figure 4 shows the microstructure of the experimental alloy and the results of EDS analysis at four points.

As indicated by the data in Table 4 and the corresponding spectrum, the structure contains Fe, Cr, Mn, Co, and Ni, with concentrations closely matching those determined by the Poly Spec-F.

The microstructure of the experimental alloy is characterised by a solid solution, presumably of the substitutional type with an f.c.c. lattice [4]. The matrix also contains minor inclusions, presumably of silicate nature.

Table 4 presents the concentrations of chemical elements in the selected spectra.

Spectrum 5 (inclusion) differs in composition from the other spectra and is the only one containing silicon while lacking other elements entirely. Analysis of the inclusion in Fig. 5 revealed that it is likely of silicate nature, originating from the presence of silicon in the feedstock materials.

Silicate-type inclusions are undesirable in the matrix, as they disrupt its homogeneity and may act as a glassy phase, reducing the matrix ductility.

As a result of the conducted research, the feasibility of producing QHEAs based on the FeCrMnNiCo system with partial substitution of pure metals by ferroalloys was confirmed. The properties of the experimental alloy are comparable to those of QHEAs based on a similar system pro-

duced entirely from pure metals with fivefold remelting. This suggests that the experimental alloy holds promise for further research aimed at improving its properties for industrial applications.

5. Conclusions

Based on the conducted research, the following conclusions can be drawn:

• high-entropy alloys exhibit significant potential for use in a wide range of industrial applications;

• an optimal balance between strength and ductility has not yet been achieved in HEAs;

• the production technologies for HEAs are quite diverse, ranging from conventional melting to the relatively rare method of melt spinning;

• compared to traditional amorphous alloys, high-entropy amorphous alloys demonstrate better thermal stability but reduced glass-forming ability;

• a relatively small number of studies have addressed HEAs with non-equiatomic compositions;

• eutectic high-entropy alloys, such as $AlCoCrFeNi_{2.1}$, demonstrate significant potential for high-temperature applications;

• the feasibility of producing quasi-high-entropy alloys while maintaining the key properties typical of HEAs based on the FeCrMnNiCo system has been confirmed, using partial substitution of pure metals with ferroalloys, which significantly reduces the cost of such alloys.

Acknowledgment. This research was funded by the Committee of Science of the Ministry of Science and Higher Education of the Republic of Kazakhstan (grant number BR24993020).

REFERENCES

1. D.B. Miracle and O.N. Senkov, A critical review of high entropy alloys and related concepts, *Acta Mater.*, **122**: 448 (2017); https://doi.org/10.1016/j.actamat.2016.08.081
2. J.-W. Yeh, Recent progress in high entropy alloys, *Ann. Chim. Sci. Mat.*, **31**, No. 7: 633 (2006); https://doi.org/10.3166/acsm.31.633-648
3. D.B. Miracle, B. Majumdar, K. Wertz, and S. Gorsse, New strategies and tests to accelerate discovery and development of multi-principal element structural alloys, *Scr. Mater.*, **127**: 1 (2016); https://doi.org/10.1016/j.scriptamat.2016.08.001
4. B.S. Murty, J.W. Yeh, and S. Ranganathan, *High-Entropy Alloys* (Oxford: Butterworth-Heinemann: 2014), p. 218; https://doi.org/10.1016/B978-0-12-800251-3.00002-X
5. J.-W. Yeh, S.-K. Chen, S.-J. Lin, J.-Y. Gan, Ts.-Sh. Chin, T.-Ts. Shun, Ch.-H. Tsau, and Sh.-Y. Chang, Nanostructured high-entropy alloys with multiple principle elements: novel alloy design concepts and outcomes, *Adv. Eng. Mater.*, **6**, No. 8: 299 (2004); https://doi.org/10.1002/adem.200300567

6. S. Ranganathan, Alloyed pleasures: Multimetallic cocktails, *Curr. Sci.*, **85**, No. 10: 1404 (2003).
7. A. Takeuchi and A. Inoue, Mixing enthalpy of liquid phase calculated by Miedema's scheme and approximated with sub-regular solution model for assessing forming ability of amorphous and glassy alloys, *Intermetallics*, **18**, No. 9: 1779 (2010); https://doi.org/10.1016/j.intermet.2010.06.003
8. L.A. Dominguez, R. Goodall, and I. Todd, Prediction and validation of quaternary high entropy alloys using statistical approaches, *Mater. Sci. Technol.*, **31**, No. 10: 1201 (2015); https://doi.org/10.1179/1743284715Y.0000000019
9. A. Takeuchi, K. Amiya, T. Wada, K. Yubuta, and W. Zhang, High-entropy alloys with a hexagonal close-packed structure designed by equi-atomic alloy strategy and binary phase diagrams, *JOM*, **66**, No. 10: 1984 (2014); https://doi.org/10.1007/s11837-014-1085-x
10. Y. Zhang, T.T. Zuo, Z. Tang, M.C. Gao, K.A. Dahmen, P.K. Liaw, and Z.P. Lu, Microstructures and properties of high-entropy alloys, *Prog. Mater. Sci.*, **61**: 1 (2014); https://doi.org/10.1016/j.pmatsci.2013.10.001
11. B. Cantor, Multicomponent and high entropy alloys, *Entropy*, **16**, No. 9: 4749 (2014); https://doi.org/10.3390/e16094749
12. C.-J. Tong, Y.-L. Chen, J.-W. Yeh, S.-J. Lin, S.-K. Chen, T.-T. Shun, C.-H. Tsau, and S.-Y. Chang, Microstructure characterization of AlCoCrCuFeNi high-entropy alloy system with multiprincipal elements, *Metall. Mater. Trans. A*, **36**, No. 4: 881 (2005); https://doi.org/10.1007/s11661-005-0283-0
13. A. Gali and E.P. George, Tensile properties of high- and medium-entropy alloys, *Intermetallics*, **39**: 74 (2013); https://doi.org/10.1016/j.intermet.2013.03.018.7
14. J.-W. Yeh, Recent Progress in High Entropy Alloys, *Ann. Chim. Sci. Mat.*, **31**, No. 7: 633 (2006); https://doi.org/10.3166/acsm.31.633-648
15. C.-J. Tong, M.-R. Chen, S.-K. Chen, J.-W. Yeh, T.-T. Shun, S.-J. Lin, and S.-Y. Chang, Mechanical performance of the AlxCoCrCuFeNi high-entropy alloy system with multiprincipal elements, *Metall. Mater. Trans. A*, **36A**, No. 5: 1263 (2005); https://doi.org/10.1007/s11661-005-0218-9
16. M.-H. Tsai and J.-W. Yeh, High-entropy alloys: a critical review, *Mater. Res. Lett.*, **2**, No. 3: 107 (2014); https://doi.org/10.1080/21663831.2014.912690
17. J.-W. Yeh, Y.-L. Chen, S.-J. Lin, and S.-K. Chen, High-entropy alloys — a new era of exploitation, *Mater. Sci. Forum*, **560**: 1 (2007); https://doi.org/10.4028/www.scientific.net/MSF.560.1
18. Y. Zhang, X. Yang, and P.K. Liaw, Alloy design and properties optimization of high-entropy alloys, *JOM*, **64**, No. 7: 830 (2012); https://doi.org/10.1007/s11837-012-0366-5
19. B. Cantor, I.T.H. Chang, P. Knight, and A.J.B. Vincent, Microstructural development in equiatomic multicomponent alloys, *Mater. Sci. Eng. A*, **375–377**: 213 (2004); https://doi.org/10.1016/j.msea.2003.10.257
20. C.C. Tung, J.W. Yeh, T.T. Shun, S.-K. Chen, Y.-S. Huang, and H.-C. Chen, On the elemental effect of AlCoCrCuFeNi high-entropy alloy system, *Mater. Lett.*, **61**, No. 1: 1 (2007); https://doi.org/10.1016/j.matlet.2006.03.140

21. V. Braic, A. Vladescu, M. Balaceanu, C.R. Luculescu, and M. Braic, Nanostructured multi-element (TiZrNbHfTa)C hard coatings, *Surf. Coat. Technol.*, **211**: 117 (2012); https://doi.org/10.1016/j.surfcoat.2011.09.033
22. S. Lei, S. Guo, E. Khosravi, and X. Yang, The Stability and Stiffness of TaNbHfZrTi Alloy from First Principles Simulation, *MS&T 2012 Proc.* (Pittsburgh: AISTECH, 2012), p. 196.
23. L. Lilensten, J.P. Couzinie, L. Perriere, J. Bourgon, N. Emery, and I. Guillot, New structure in refractory high-entropy alloys, *Mater. Lett.*, **132**: 123 (2014); https://doi.org/10.1016/j.matlet.2014.06.064
24. C.M. Liu, H.M. Wang, S.Q. Zhang, H.B. Tang, and A.L. Zhang, Microstructure and oxidation behavior of new refractory high entropy alloys, *J. Alloys Compd.*, **583**: 162 (2014); https://doi.org/10.1016/j.jallcom.2013.08.102
25. O.N. Senkov, S.V. Senkova, D.M. Dimiduk, C. Woodward, and D.B. Miracle, Oxidation behavior of a refractory $NbCrMo_{0.5}Ta_{0.5}TiZr$ alloy, *J. Mater. Sci.*, **47**, No. 18: 6522 (2012); https://doi.org/10.1007/s10853-012-6582-0
26. O.N. Senkov, S.V. Senkova, and C. Woodward, Effect of aluminum on the microstructure and properties of two refractory high entropy alloys, *Acta Mater.*, **68**: 214 (2014); https://doi.org/10.1016/j.actamat.2014.01.029
27. V.H. Hammond, M.A. Atwater, K.A. Darling, H.Q. Nguyen, and L.J. Kecskes, Equal-channel angular extrusion of a low-density high-entropy alloy produced by high-energy cryogenic mechanical alloying, *JOM*, **66**, No. 10: 2021 (2014); https://doi.org/10.1007/s11837-014-1113-x
28. X. Yang, S.Y. Chen, J.D. Cotton, and Y. Zhang, Phase stability of low-density, multiprincipal component alloys containing aluminum, magnesium, and lithium, *JOM*, **66**, No. 10: 2009 (2014); https://doi.org/10.1007/s11837-014-1059-z
29. K.M. Youssef, A.J. Zaddach, C. Niu, D.L. Irving, and C.C. Koch, A novel low density, high hardness, high-entropy alloy with close-packed single-phase nanocrystalline structures, *Mater. Res. Lett.*, **3**, No. 2: 95 (2014); https://doi.org/10.1080/21663831.2014.985855
30. B. Cantor, K.B. Kim, and P.J. Warren, Novel multicomponent amorphous alloys, *Mater. Sci. Forum*, **386–388**: 27 (2002); https://doi.org/10.4028/www.scientific.net/MSF.386-388.27
31. K.-H. Cheng, C.-H. Lai, S.-J. Lin, and J.-W. Yeh, Recent progress in multi-element alloy and nitride coatings sputtered from high-entropy alloy targets, *Ann. Chim. Sci. Mat.*, **31**, No. 7: 723 (2006); https://doi.org/10.3166/acsm.31.723-736
32. K.-H. Cheng, C.-H. Lai, S.-J. Lin, and J.-W. Yeh, Structural and mechanical properties of multi-element $(AlCrMoTaTiZr)N_x$ coatings by reactive magnetron sputtering, *Thin Solid Films*, **519**, No. 10: 3185 (2011); https://doi.org/10.1016/j.tsf.2010.11.034
33. M.-H. Hsieh, M.-H. Tsai, W.-J. Shen, and J.-W. Yeh, Structure and properties of two Al-Cr-Nb-Si-Ti high-entropy nitride coatings, *Surf. Coat. Technol.*, **221**: 118 (2013); https://doi.org/10.1016/j.surfcoat.2013.01.036
34. H.-T. Hsueh, W.-J. Shen, M.-H. Tsai, and J.-W. Yeh, Effect of nitrogen content and substrate bias on mechanical and corrosion properties of high-entropy films $(AlCrSiTiZr)_{100-x}N_x$, *Surf. Coat. Technol.*, **206**, Nos. 19–20: 4106 (2012); https://doi.org/10.1016/j.surfcoat.2012.03.096

35. V. Braic, A. Vladescu, M. Balaceanu, C.R. Luculescu, and M. Braic, Nanostructured multi-element (TiZrNbHfTa)N and (TiZrNbHfTa)C hard coatings, *Surf. Coat. Technol.*, **211**: 117 (2012);
https://doi.org/10.1016/j.surfcoat.2011.09.033
36. C.-Y. Hsu, J.-W. Yeh, S.-K. Chen, and T.-T. Shun, Wear resistance and high-temperature compression strength of FCC CuCoNiCrAl0.5Fe alloy with boron addition, *Metall. Mater. Trans. A*, **35**, No. 5: 1465 (2004);
https://doi.org/10.1007/s11661-004-0254-x
37. L. Yang, Y. Li, Z. Wang, W. Zhao, and C. Qin, Nanoporous Quasi-High-Entropy Alloy Microspheres, *Metals*, **9**, No. 3: 345 (2019);
https://doi.org/10.3390/met9030345
38. C.-M. Lin and H.-L. Tsai, Effect of annealing treatment on microstructure and properties of high-entropy FeCoNiCrCu0.5 alloy, *Mater. Chem. Phys.*, **128**, Nos. 1–2: 50 (2011);
https://doi.org/10.1016/j.matchemphys.2011.02.022
39. C. Li, J.C. Li, M. Zhao, and Q. Jiang, Effect of alloying elements on microstructure and properties of multiprincipal elements high-entropy alloys, *J. Alloys Compd.*, **475**, Nos. 1–2: 752 (2009);
https://doi.org/10.1016/j.jallcom.2008.07.124
40. H.B. Cui, L.F. Zheng, and J.Y. Wang, Microstructure evolution and corrosion behavior of directionally solidified FeCoNiCrCu high entropy alloy, *Appl. Mech. Mater.*, **66–68**: 146 (2011);
https://doi.org/10.4028/www.scientific.net/AMM.66-68.146
41. J. Gu, S. Ni, Y. Liu, and M. Song, Regulating the strength and ductility of a cold rolled FeCrCoMnNi high-entropy alloy *via* annealing treatment, *Mater. Sci. Eng. A*, **755**: 289 (2019);
https://doi.org/10.1016/j.msea.2019.04.025
42. X. Ma, J. Chen, X. Wang, Y. Hu, and Y. Hue, Microstructure and mechanical properties of cold drawing CoCrFeMnNi high entropy alloy, *J. Alloys Compd.*, **795**: 45 (2019);
https://doi.org/10.1016/j.jallcom.2019.04.296
43. Z. Zhang, J. Liang, S.L.I. Chan, J. Ju, Y. Zhou, and J. Wang, Synergistic strengthening mechanisms and multiple deformation behaviors of in-situ synthesized Al_2O_3 nanoparticles reinforced $CoCrFeNiAl_{0.3}$ high entropy alloy matrix nanocomposite with heterogeneous microstructure, *Mater. Sci. Eng. A*, **924**: 147785 (2025);
https://doi.org/10.1016/j.msea.2025.147785
44. I. Moravcik, J. Cizek, J. Zapletal, Z. Kovasova, J. Vesely, P. Minarik, M. Kitzmantel, E. Neubauer, and I. Dlouhy, Microstructure and mechanical properties of $Ni_{1.5}Co_{1.5}CrFeTi_{0.5}$ high entropy alloy fabricated by mechanical alloying and spark plasma sintering, *Mater. Des.*, **119**: 141 (2017);
https://doi.org/10.1016/j.matdes.2017.01.036
45. K. Guo, Y. Zhang, C. Chen, Y. Tu, M. Chang, and E. Tang, Discharge and ignition mechanism of high-entropy alloy induced by crack propagation under quasi-static compressive load, *Intermetallics*, **170**: 108312 (2024);
https://doi.org/10.1016/j.intermet.2024.108312
46. F. Prusa, A. Senkova, V. Kusera, J. Capek, and D. Vojtech, Properties of high-strength ultrafine-grained CoCrFeNiMn high-entropy alloy prepared by short-term mechanical alloying and spark plasma sintering, *Mater. Sci. Eng. A*, **734**: 341 (2018);
https://doi.org/10.1016/j.msea.2018.08.014
47. V. Dolique, A.L. Thomann, and P. Brault, High-entropy alloys deposited by magnetron sputtering, *IEEE Trans. Plasma Sci.*, **39**, No. 11: 2478 (2011);
https://doi.org/10.1109/TPS.2011.2157942

48. H.W. Chang, P.K. Huang, J.W. Yeh, A. Davison, C.H. Tsau, and C.C. Yang, Influence of substrate bias, deposition temperature and post-deposition annealing on the structure and properties of multi-principal-component (AlCrMoSiTi)N coatings, *Surf. Coat. Technol.*, **202**: 3360 (2008);
https://doi.org/10.1016/j.surfcoat.2007.12.014
49. H.N. Trofimenko, I.Yu. Efimochkin, and A.N. Bolshakova, *Aviats. Mater. Tekhnol.*, No. 2 (51): 3 (2018).
50. Y. Geng, S.V. Konovalov, and X. Chen, Research status and application of the high-entropy and traditional alloys fabricated *via* the laser cladding, *Prog. Phys. Met.*, **21**, No. 1: 26–45 (2020);
https://doi.org/10.15407/ufm.21.01.026
51. A.V. Zavdoveev, T. Baudin, D.G. Mohan, D.L. Pakula, D.V. Vedel, and M.A. Skoryk, Basics of additive manufacturing processes for high-entropy alloys, *Prog. Phys. Met.*, **24**, No. 3: 561–592 (2023);
https://doi.org/10.15407/ufm.24.03.561
52. S.V. Maksymova and V.E. Sukhoyars'kyy, Structure of high-entropy solders and soldered seams based on transition *d*-metals, *Metallofiz. Noveishie Tekhnol.*, **45**, No. 1: 75–93 (2023);
https://doi.org/10.15407/mfint.45.01.0075
53. K. Chong, Y. Gao, Z. Zhang, X. Liang, and Y. Zou, Glass forming ability and thermal stability of $(ZrTiHfNi)_{100-x}Nbx$ high entropy amorphous alloy, *J. Mater. Res. Technol.*, **36**: 699 (2025);
https://doi.org/10.1016/j.jmrt.2025.03.132
54. W. Gao, M. Feng, C. Chen, and G. Lian, Microstructure evolution, wear resistance and corrosion resistance of $CoCrCu_{0.5}FeNiSi_x$ high-entropy alloy coatings fabricated by laser cladding, *J. Mater. Res. Technol.*, **36**: 5539 (2025);
https://doi.org/10.1016/j.jmrt.2025.04.210
55. Z. Wang, F. Xing, G. Xu, W. Liu, and H. Bian, Microstructure and mechanical properties of additive manufactured TiC-reinforced $Fe_{55}Cr_{25}Co_{10}Ni_{10}$ high-entropy alloy composites, *Opt. Laser Technol.*, **187**: 112870 (2025);
https://doi.org/10.1016/j.optlastec.2025.112870
56. B.-S. Lou, C.-L. Li, M. Annalakshmi, T.-Y. Hung, and J.-W. Lee, Exploring the effect of Ti and Al contents on the microstructural, mechanical, and corrosion resistance features of VNbMoTaWTiAlN refractory high entropy alloy coatings, *Mater. Chem. Phys.*, **341**: 130901 (2025);
https://doi.org/10.1016/j.matchemphys.2025.130901
57. F. Li, R. Liu, K. Ma, Y. Zhao, X. Fu, X. Zhang, Y. Ling, and J. Li, Tensile properties and molecular dynamics simulation of $FeCrMnAl_xCu$ high-entropy alloys, *Vacuum*, **238**: 114219 (2025);
https://doi.org/10.1016/j.vacuum.2025.114219
58. Y. Yin, J. Hu, X. Xu, Q. Yang, Y. Zhang, D. Yan, and Z. Li, Microstructural evolution and mechanical behavior of (WMoNbVTa)C–Co high-entropy cemented carbides: The role of Ta alloying, *J. Alloys Compd.*, **1022**: 180076 (2025);
https://doi.org/10.1016/j.jallcom.2025.180076
59. Y. Li, X. Jin, A. Lan, and J. Qiao, Superior strength-ductility synergy of FeMnCrNiAlSi high entropy alloy with heterogeneous structures, *J. Alloys Compd.*, **1025**: 180279 (2025);
https://doi.org/10.1016/j.jallcom.2025.180279
60. F.-C. Zhao, G.-N. Ji, X.-M. Zhao, R.-D. Zhao, and F.-F. Wu, The role of copper in transforming CuxCoCrNiAl high-entropy alloys for enhanced strength and ductility, *Mater. Charact.*, **223**: 114973 (2025);

https://doi.org/10.1016/j.matchar.2025.114973
61. H. Yang, Z. Zeng, T. Xiong, Z. Shao, Q. Lu, and S. Zhang, High-temperature mechanical properties and radiation resistance properties of reduced-activation high-entropy alloys $FeMnCrTi_{0.1}$, *J. Alloys Compd.*, **1014**: 178746 (2025); https://doi.org/10.1016/j.jallcom.2025.178746
62. Y. Guo, H. Wang, X. Guo, D. Cong, J. Yang, J. Li, and Z. Li, Ultra-wide working temperature range of elastocaloric effect in a $(Ti_{25}Zr_{10}Hf_{15}Ni_{25}Cu_{25})_{99.6}B_{0.4}$ high entropy shape memory alloy, *J. Alloys Compd.*, **1021**: 179683 (2025); https://doi.org/10.1016/j.jallcom.2025.179683
63. Y. Li, S. Liang, J. Gong, W. Wu, Y. Wang, and Z. Chen, Effect of Ti on the structure and mechanical properties of Ti_xVNbMo (x = 0.5, 1.0, 1.5, 2.0) refractory high-entropy alloys: A combined first principles and experimental study, *Intermetallics*, **181**: 108760 (2025); https://doi.org/10.1016/j.intermet.2025.108760
64. Y. Heidari, Kh. Gheisari, and M. Yeganeh, Effect of Cr content on the structure and corrosion properties of $(FeCoNi)_{0.75}Cu_{0.25-x}Cr_x$ high entropy alloys in 1 M H_2SO_4, *J. Mater. Res. Technol.*, **35**: 5322 (2025); https://doi.org/10.1016/j.jmrt.2025.02.184
65. C. Che, M. Jiang, A. Li, K. Kang, J. Zhang, D. Huang, and G. Li, Effect of Ni content on the corrosion resistance of $CoCr_{0.8}FeTi_{0.4}Ni_x$ high entropy alloys in 3.5 wt% NaCl solution, *J. Alloys Compd.*, **1016**: 178900 (2025); https://doi.org/10.1016/j.jallcom.2025.178900
66. Z. Li, W. Wang, X. Chen, B. Peng, H. Xing, and J. Yang, Effect of the addition of Sc element on the microstructure and properties of $Al_{80}Li_5Mg_5Zn_5Cu_5$ high-entropy alloy, *J. Mater. Res. Technol.*, **34**: 1436 (2025); https://doi.org/10.1016/j.jmrt.2024.12.074
67. X. Zhang, P. Bai, F. Wang, H. Zhao, X. Zhou, S. Wang, J. Gao, C. Zhang, H.-H. Wu, and X. Mao, Atomistic insight into the effects of W content on the creep behaviors of NbMoTaW high-entropy alloys, *J. Mater. Res. Technol.*, **36**: 3289 (2025); https://doi.org/10.1016/j.jmrt.2025.03.298
68. S. Liu, B. Dou, S. Sun, L. Wang, Y.-J. Liang, and Y. Xue, Simultaneous improvement in strength and ductility of 3D-printed refractory high-entropy alloys by addition of molybdenum, *Mater. Sci. Eng. A*, **928**: 148042 (2025); https://doi.org/10.1016/j.msea.2025.148042
69. K. Sikdar, A. Mahata, C. Chattopadhyay, D. Roy, and R. Mitra, Influence of Y (yttrium) doping on thermal stability of nanocrystalline AlCoCrCuFeNi high entropy alloy, *Intermetallics*, **179**: 108638 (2025); https://doi.org/10.1016/j.intermet.2025.108638
70. J.-D. Zhang, L. Zhang, H.Z. Ma, and N. Li, Effects of ZrC content on microstructures and properties of ZrC/AlCoCrFeNi high-entropy alloys composites, *J. Alloys Compd.*, **1010**: 178308 (2025); https://doi.org/10.1016/j.jallcom.2024.178308
71. P. Gao, K. Wang, Y. Sheng, T. Cui, F. Li, Z. Wang, Y. Fu, F. Dai, S. Chen, B. Li, and H. Guo, Microstructure and properties of laser-cladded $CoCrMoNb(TiC)_x$ high entropy alloy coatings with various TiC contents, *Surf. Coat. Technol.*, **505**: 132116 (2025); https://doi.org/10.1016/j.surfcoat.2025.132116
72. Q. Huang, Y. Li, P. Zhang, Y. Yang, S. Zhou, P. Ren, Q. Wang, W. Li, and F. Wang, The oxidation mechanisms of Pt and reactive elements modified $AlCoCrFeNi_{2.1}$ eutectic high-entropy alloy at high temperature, *J. Mater. Res. Technol.*, **36**: 4602 (2025); https://doi.org/10.1016/j.jmrt.2025.04.138

73. Y.-Y. Tan, J.-X. Chen, M.-Y. Su, T. Li, Z.-J. Chen, Y. Chen, H.-Y. Wang, D.-S. Wu, Z.-J. Tan, H.-L. Lu, L.-H. He, and L.-H. Dai, Insight into the local atomic structure effects on deformation behavior of high entropy alloys by in-situ neutron diffraction and EXAFS, *Mater. Sci. Eng. A*, **932**: 148231 (2025); https://doi.org/10.1016/j.msea.2025.148231
74. Y. Tang, F. Zhang, Y. Xiong, Y. Hu, and H. Feng, Interface microstructure and strengthening mechanisms of medium-entropy alloy FeCoNiCr particle reinforced titanium composites, *Mater. Sci. Eng. A*, **935**: 148359 (2025); https://doi.org/10.1016/j.msea.2025.148359
75. Z. Yang, H.T. He, J.X. Fang, T. Sun, B. Ma, H.T. Chen, T. Fu, J.T. Wei, M. Wen, and P. He, Microstructure and mechanical properties of carbide-reinforced Ta-W-based refractory medium-entropy alloys prepared by spark plasma sintering, *Int. J. Refract. Met. Hard Mater.*, **130**: 107182 (2025); https://doi.org/10.1016/j.ijrmhm.2025.107182
76. L. Yu, Y.-Q. Yan, W.-T. Zhang, H. Zhang, J. Wu, C. Liu, L. Yao, J. Lu, and G. Wu, Grain size effect on corrosion behaviour of TiZrNb medium-entropy alloys, *J. Alloys Compd.*, **1025**: 180338 (2025); https://doi.org/10.1016/j.jallcom.2025.180338
77. G.M. Pillai, K. Singh, S. Thangaraju, S. Jha, and V. Kumar, Corrosion and wear study of medium entropy Pb–Sn–Cu alloy for coating application, *J. Alloys Metall. Syst.*, **9**: 100156 (2025); https://doi.org/10.1016/j.jalmes.2025.100156
78. D. Wu, B. Li, Y. Shi, X. Hou, C. Li, Y. Gao, P. Bai, Y. Liu, and C. Liang, Effects of different Al contents on mechanical properties and high temperature oxidation resistance of $Al_xCoCr_{0.6}NiV_{0.6}$ high entropy alloy, *J. Alloys Compd.*, **1025**: 180348 (2025); https://doi.org/10.1016/j.jallcom.2025.180348
79. S.V. Maksymova, V.V. Voronov, and P.V. Kovalchuk, Influence of adhesive-active components on thermodynamic parameters of high-entropy NiCoCrAl–(Ti, Nb) Brazing Filler Metals, *Metallofiz. Noveishie Tekhnol.*, **46**, No. 8: 811–823 (2024); https://doi.org/10.15407/mfint.46.08.0811
80. V.S. Klochko, A.V. Korniyets, I.V. Kolodiy, O.O. Kondratov, V.I. Sokolenko, V.I. Spitsyna, T.M. Tykhonovska, and N.A. Yayes, Ultrasonic investigation of high-entropy $Al_{0.5}CoCrCuFeNi$ alloy at low temperature, *Metallofiz. Noveishie Tekhnol.*, **45**, No. 4: 523–535 (2023); https://doi.org/10.15407/mfint.45.04.0523
81. R. Liu, R. Lu, A. Wang, Z. Zhu, and H. Wang, First-principles study on local site preference of interstitial oxygen in $Ti_3Zr_{1.5}NbVAl_{0.25}$ high-entropy alloy, *Comput. Mater. Sci.*, **253**: 113867 (2025); https://doi.org/10.1016/j.commatsci.2025.113867
82. J.M. Torralba, A. Meza, S.V. Kumaran, A. Mostafaei, and A. Mohammadzadeh, From high-entropy alloys to alloys with high entropy: A new paradigm in materials science and engineering for advancing sustainable metallurgy, *Curr. Opin. Solid State Mater. Sci.*, **36**: 101221 (2025); https://doi.org/10.1016/j.cossms.2025.101221
83. Z. Yang, S. Wang, R. Cao, W. Tang, J. Chen, J. Li, J. Wang, Z. Wang, and F. He, Abnormal recrystallization kinetics of precipitation-hardened high-entropy alloys, *Rev. Mater. Res.*, 1, No. 2: 100037 (2025); https://doi.org/10.1016/j.revmat.2025.100037
84. G. Abrantes, B. Alves, D. Gatxes, R. Batalha, and P.F. Rodrigues, Design of non-equiatomic low-density alloys inspired by modified high-entropy shape memory alloy,

J. Mater. Res. Technol., **36**: 72 (2025);
https://doi.org/10.1016/j.jmrt.2025.02.059
85. G.-Y. Wang, W.-C. Hsu, Z.-W. Huang, J.-W. Yeh, and C.-W. Tsai, The growth activation energy of sigma phase in nonequal molar CoCrFeNiV low entropy and high entropy alloys, *J. Alloys Compd.*, **1017**: 178863 (2025);
https://doi.org/10.1016/j.jallcom.2025.178863
86. Z. Zhang, Y. Meng, Z. Zhang, Y. Yang, Y. Chen, C. Wang, and Y. He, Predictive and heuristic framework for high entropy alloys design: Integrating solid solution strengthening with machine learning, *J. Alloys Compd.*, **1027**: 180484 (2025);
https://doi.org/10.1016/j.jallcom.2025.180484
87. X.-Y. Song, H.-L. Zhao, W. Cheng, X.-G. Li, J.-P. Zhu, Y. Zhang, G. Liu, and X.-B. Liu, Atomic-scale insight into the effect of graphene on the tribological behavior of high-entropy alloys, *Mater. Lett.*, **387**: 138252 (2025);
https://doi.org/10.1016/j.matlet.2025.138252
88. S.V. Maksymova, V.V. Voronov, and P.V. Kovalchuk, High-entropy brazing filler metal based on NiCoCrPdGe system for brazing nickel superalloys, *Metallofiz. Noveishie Tekhnol.*, **45**, No. 3: 387 (2023);
https://doi.org/10.15407/mfint.45.03.0387
89. D. Li, H. Shi, D. Liang, Z. Liang, L. Zhang, W. Ding, and X. Su, Microstructural evolution and mechanical properties of CrCoFeMnNi high-entropy alloys under femtosecond laser ablation: a molecular dynamics approach, *J. Mater. Res. Technol.*, **35**: 6333 (2025);
https://doi.org/10.1016/j.jmrt.2025.02.247
90. Q. Lin and Y. Yan, Hydrogen storage properties of VNbTaTi and VNbTaTiAl high-entropy alloys: A first principles study, *Vacuum*, **238**: 114286 (2025);
https://doi.org/10.1016/j.vacuum.2025.114286
91. B.A. Rusanov, E.V. Sterkhov, A.I. Rusanova, and D.K. Simonov, The Laves phase formation in rapidly quenched Zr–Al–Ni–Co–Cu high-entropy alloy, *J. Alloys Metall. Syst.*, **9**: 100165 (2025);
https://doi.org/10.1016/j.jalmes.2025.100165
92. H. Li, D. Zhou, P.E.S. Smith, E. Sharman, H. Xiao, S. Wang, Y. Huang, and J. Jiang, Spectra-based clustering of high-entropy alloy catalysts: improved insight over use of atomic structure, *Chem. Sci.*, **16**, No. 11: 4646 (2025);
https://doi.org/10.1039/d4sc06552b
93. Y. Lu, X. Wu, F. Zhang, F. Sun, and X. Dong, Comparative analysis of additive manufacturing techniques and microstructural strengthening mechanisms in $Al_{0.3}CoCrFeNiTi_{0.15}$ high entropy alloy, *Mater. Sci. Eng. A*, **934**: 148303 (2025);
https://doi.org/10.1016/j.msea.2025.148303
94. Z. Dastjerdi, M. Sharifitabar, and M.S. Afarani, Effect of Cr_2O_3 purity on the microstructure and hardness of AlTiVCr high entropy alloy prepared by self-propagating high-temperature synthesis, *Mater. Chem. Phys.*, **341**: 130942 (2025);
https://doi.org/10.1016/j.matchemphys.2025.130942
95. R. Mu, Y. Wang, S. Niu, K. Sun, and Z. Yang, Stabilized interfacial structure induced by self-dissolved active atoms in the (HfZrTiTaNb)C high-entropy carbide brazed joint using CoCrFeNi alloy, *Ceramics International*, **51**, Iss. 15: 20006 (2025);
https://doi.org/10.1016/j.ceramint.2025.02.165
96. S. Jain, R. Jain, V. Kumar, S. Samal, and J. Lee, Design strategies and mechanical behaviour of high-strength eutectic high-entropy alloys: a comprehensive review, *J. Alloys Compd.*, **1022**: 180000 (2025);
https://doi.org/10.1016/j.jallcom.2025.180000

97. C. Wang, X. Yang, X. Sun, H. Kang, and P. Xiao, First-principles and experimental study on structure and properties of $CuCrCoFeNi_xTi$ high entropy alloy, *Intermetallics*, **181**: 108735 (2025); https://doi.org/10.1016/j.intermet.2025.108735
98. K. Chakrabarty, A.D. Pope, A. Yadav, W. Yang, J. Ren, V. Rangari, W. Chen, and Y.K. Vohra, High-pressure high-temperature melting and recrystallization of nanolamellar high-entropy alloys, *J. Alloys Compd.*, **1020**: 179470 (2025); https://doi.org/10.1016/j.jallcom.2025.179470
99. H.M. Wang, S.S. Chou, T.T. Wu, G.R. Li, Z.J. Ji, and X. Zong, Microstructure and properties of $Fe_{20}Co_{20}Ni_{40}Al_{20}$ high-entropy alloy enhanced *via* deep cryogenic treatment, *J. Mater. Res. Technol.*, **36**: 3177 (2025); https://doi.org/10.1016/j.jmrt.2025.04.017
100. R. Sun, H. Yin, J. Liu, S. Xie, C. Zhang, R. Zhang, Y. Wang, D.F. Khan, and X. Qu, Screening the TiZrHfNbVMoTa refractory high-entropy alloys with multiproperty constraints, *J. Alloys Compd.*, **1020**: 179284 (2025); https://doi.org/10.1016/j.jallcom.2025.179284
101. Y. Xu, D. Wang, S. Wu, H. Lu, R. Yao, J. Yang, F. Jiang, and T. Akiyama, Research progress on defect formation mechanism and process optimization of laser cladding high entropy alloy coatings, *Opt. Laser Technol.*, **187**: 112819 (2025); https://doi.org/10.1016/j.optlastec.2025.112819
102. K. Yu, Z. Li, F. Zhou, Y. Li, J. Tang, and Z. Luo, Effect of C content on the microstructural evolution and wear resistance of AlCoCrFeNiTiW high-entropy alloy coatings, *Surf. Coat. Technol.*, **505**: 132115 (2025); https://doi.org/10.1016/j.surfcoat.2025.132115
103. M. Zhang, Y. Wang, Y. Zhou, D. Wang, X. Yang, D. Cheng, A.U.H. Mohsan, J. Tang, and G. Zhang, Surface morphology evolution and tribological properties of laser directed energy deposited CoCrFeNi high-entropy alloys using laser polishing, *J. Alloys Compd.*, **1022**: 179893 (2025); https://doi.org/10.1016/j.jallcom.2025.179893
104. J. Guo, W. Xie, and J. Pu, Tribocorrosion behaviors and mechanisms of in-situ $TiC/TiB/Cr_2B$ reinforced CrMnFeCoNi high-entropy alloy composite coatings prepared by laser cladding, *Ceramics International*, **51**, Iss. 18, Pt. B: 26742 (2025); https://doi.org/10.1016/j.ceramint.2025.03.355
105. A.V. Zavdoveev, O.A. Gaivoronsky, V.D. Poznyakov, A.V. Klapatyuk, D.V. Vedel, T. Baudin, O.A. Los, R.A. Kozin, and M.A. Skoryk, Powder welding wire of Cantor's high-entropy alloying system for surfacing, *Metallofiz. Noveishie Tekhnol.*, **44**, No. 8: 1025 (2022); https://doi.org/10.15407/mfint.44.08.1025
106. Y. Zeng, Y. He, T. Dou, J. Yang, J. Li, J. Jiang, C. Ying, M. Zheng, C. Tan, and H. Zhang, Dissimilar laser joining of aluminum to steel *via* a porous FeCoCrNi high entropy alloy coating: Interfacial microstructure, wettability, and mechanical properties, *Appl. Surf. Sci.*, **694**: 162809 (2025); https://doi.org/10.1016/j.apsusc.2025.162809
107. Y. Ruan, C. Yin, X. Liu, D. Zhang, J. Wu, and Z. Zhu, A cobalt-free dual-phase FeCrNiMoSi high-entropy alloy coating with high wear and corrosion resistance compared with FeCoCrNi, *J. Alloys Compd.*, **1024**: 180183 (2025); https://doi.org/10.1016/j.jallcom.2025.180183
108. H.A. Bagliuk, M.V. Marich, S.F. Kirilyuk, O.M. Myslivchenko, O.A. Golubenko, and O.S. Makarenko, Comparative analysis of the structure, phase composition and properties of high-entropy cermets of Ti–Cr–Fe–Ni–C system obtained by powder metallurgy and arc remelting methods, *Metallofiz. Noveishie Tekhnol.*,

45, No. 4: 537 (2023);
https://doi.org/10.15407/mfint.45.04.0537
109. F. Yang, C. Du, S. Tao, Y. Chang, Z. Nie, Z. Wang, and H. Lu, Study on the effect and growth mechanism of micro-arc oxidation coating on AlCoCrFeNi high entropy alloy, *J. Alloys Compd.*, **1020**: 179469 (2025);
https://doi.org/10.1016/j.jallcom.2025.179469
110. M.D. Le, T.H. Nguyen, V.D. Nguyen, M.K. Pham, and H.H. Nguyen, The effect of microstructure on mechanical and magnetic properties of $FeCoNiAl_{0.75}Nb_{0.25}$ high-entropy alloy, *RSC Adv.*, **15**, No. 9: 7172 (2025);
https://doi.org/10.1039/d5ra00358j
111. T.O. Kosorukova, Yu.M. Koval', V.V. Odnosum, V.S. Filatova, G. Gerstein, H.J. Maier, and G.S. Firstov, Structure, Phase composition and mechanical properties for the high entropy solid solutions based upon MnFeCoNiCu system versus collective behaviour of their constituents, *Metallofiz. Noveishie Tekhnol.*, **44**, No. 12: 1711 (2022);
https://doi.org/10.15407/mfint.44.12.1711
112. A.O. Perekos, B.M. Mordyuk, V.Z. Voynash, N.V. Danko, and T.G. Kabantsev, Influence of the copper content on phase composition and magnetic properties of ultra-fine powders of $AlCoCrCu_xFeNi$ (x = 0, 1, 2) high-entropy alloys produced by ultrasonic ball milling, *Metallofiz. Noveishie Tekhnol.*, **44**, No. 9: 1213 (2022);
https://doi.org/10.15407/mfint.44.09.1213
113. C. Xu, Q. Shen, S. Feng, F. Li, M. Liu, X. Wang, and W. Liu, Effect of aging treatment on the microstructure and mechanical properties of $Al_{0.4}Cr_{0.7}FeNi_2V_{0.2}$ high entropy alloy, *Mater. Today Commun.*, **45**: 112296 (2025);
https://doi.org/10.1016/j.mtcomm.2025.112296
114. M. Zhao, J. Wang, H. Li, H. Yang, Y. Zhou, and J. Li, Grain size effects on mechanical behavior of $Al_{0.25}CoCrFeNi$ high-entropy alloy at room and cryogenic temperatures, *Intermetallics*, **183**: 108792 (2025);
https://doi.org/10.1016/j.intermet.2025.108792
115. P. Kumar, D.H. Cook, W. Wang, M. Payne, P.P.P.O. Borges, A.M. Minor, M. Asta, and R.O. Ritchie, Fracture behavior of high-entropy alloys: Resistance to fracture from strain hardening and softening, *Matter*, **8**, No. 4: 102042 (2025);
https://doi.org/10.1016/j.matt.2025.102042
116. H. Yi, C. Tao, C. Chen, J. Fan, and S. Wang, Enhanced cryogenic tensile properties in a Fe-high-entropy alloy, *J. Alloys Compd.*, **1017**: 179052 (2025);
https://doi.org/10.1016/j.jallcom.2025.179052
117. S. González, S. Wurster, C.G. Garay-Reyes, A. Hurtado-Macías, P. Ramasamy, D. Oleszak, C. Gammer, K.G. Prashanth, A. Martínez-García, J. Eckert, and R. Martínez-Sánchez, Mechanical properties of two novel non-equiatomic Zr–Hf–Ti–Cu–Ni–Co–Al high entropy alloys with high glass forming ability, *J. Alloys Compd.*, **1024**: 180196 (2025);
https://doi.org/10.1016/j.jallcom.2025.180196
118. K. Zhao, J. Wang, J. Xiao, Y. Shen, Y. Huang, and Z. Wang, Long-term stability of dual-phase FeNiAlCr high entropy alloy at 600 °C, *Phys. B Condens. Matter*, **707**: 417187 (2025);
https://doi.org/10.1016/j.physb.2025.417187
119. V.V. Girzhon, V.V. Yemelianchenko, and O.V. Smolyakov, Structure of high-entropy CoCrFeNi alloy obtained by laser Alloying, *Metallofiz. Noveishie Tekhnol.*, **44**, No. 6: 725 (2022);
https://doi.org/10.15407/mfint.44.06.0725
120. A.O. Perekos, B.N. Mordyuk, V.Z. Voynash, V.V. Bondar, Ye.O. Svystunov, D.L. Vashchuk, S.Yu. Makarenko, and T.G. Kabantsev, Structure, phase composition and

magnetic properties of ultrafine powders of high-entropy alloys of the AlCoCr-CuFeNi system with different contents of al and cr produced by ultrasonic treatment in a ball mill, *Metallofiz. Noveishie Tekhnol.*, **44**, No. 3: 311 (2022); https://doi.org/10.15407/mfint.44.03.0311

121. G.S. Firstov, Yu.M. Koval, V.S. Filatova, V.V. Odnosum, G. Gerstein, and H.J. Maier, Development of high-entropy shape-memory alloys: structure and properties, *Prog. Phys. Met.*, **24**, No. 4: 819 (2023); https://doi.org/10.15407/ufm.24.04.819
122. H. Ma, Y. Zhao, Y. Su, Z. Yu, and P.K. Liaw, Face-centered-cubic (FCC) to body-centered-cubic (BCC) phase-transformation-induced strengthening of nanoscale harmonic-like high-entropy alloys, *Mater. Chem. Phys.*, **339**: 130756 (2025); https://doi.org/10.1016/j.matchemphys.2025.130756
123. S. Kvon, A. Issagulov, V. Kulikov, and S. Arinova, Niobium's effect on the properties of a quasi-high-entropy alloy of the CoCrFeMnNi system, *Metals*, **14**, No. 5: 564 (2024); https://doi.org/10.3390/met14050564
124. S.S. Kvon, V.Y. Kulikov, A.Z. Issagulov, A.M. Dostayeva, and T.V. Kovalyova, Studying structure and properties of shaped ingots obtained in various conditions of crystallization, *Metalurgija*, **57**, No. 4: 313 (2018).
125. P.V. Kovalev, S.D. Popova, A.Z. Issagulov, V.Y. Kulikov, and S.S. Kvon, Investigation of the effect of high strength strips steel modification with rare-earth metal (REM), *Metalurgija*, **56**, Nos. 3–4: 393 (2017).
126. S.S. Kvon, A.Z. Issagulov, M.K. Ibatov, V.Y. Kulikov, and S.K. Arinova, Investigation of the properties of the CoCrFeMnNi alloy developed on the basis of the entropy approach, *Metalurgija*, **63**, Nos. 3–4: 366 (2024).

Received / Final version
18.05.2025 / 25.10.2025

С.С. Квон, В.Ю. Куликов, С.К. Арінова, А.А. Туґанбаева
Карагандинський технічний університет імені Абилкаса Сагінова,
просп. Нурсултана Назарбаєва, 56; 100003, Караганда, Казахстан

СУЧАСНИЙ СТАН ДОСЛІДЖЕНЬ У ГАЛУЗІ ВИРОБНИЦТВА ВИСОКОЕНТРОПІЙНИХ СПЛАВІВ У СВІТОВІЙ ПРАКТИЦІ

Металеві багатокомпонентні високоентропійні сплави (ВЕС) являють собою новий клас матеріалів, що наразі активно вивчаються. У статті проаналізовано еволюцію досліджень у галузі ВЕС, розглянуто потенційні напрями застосування подібних матеріалів. Розглянуто сучасні дослідження ВЕС, зокрема вплив різних елементів на властивості ВЕС з різною основою, формування мікроструктури таких матеріалів і розробки в галузі проєктування. Результати аналізу показали, що для виготовлення ВЕС використовують порошки чистих металів і застосовують досить складні технології, наприклад плазмове спікання, магнетронне розпорошення. Для зниження вартості ВЕС порівняно з традиційними матеріалами дедалі більш популярним напрямом стає створення так званих квазівисокоентропійних сплавів (КВЕС). Загальний принцип створення КВЕС такий самий, як і ВЕС: використовується багатокомпонентна система, що складається щонайменше з п'яти компонентів, проте еквіатомна концентрація дотримується нестрого, а під час виробництва КВЕС вимоги до шихти та способу плавлення значно нижчі. Це уможливлює підвищення комерційної привабливості КВЕС за рівня властивостей, які можна порівняти з властивостями ВЕС.

Ключові слова: високоентропійний сплав, квазівисокоентропійний сплав, еквіатомна концентрація, феросплави, собівартість.